AIAA JOURNAL
Vol. 54, No. 3, March 2016

Real-Gas and Surface-Ablation Effects on Hypersonic Boundary-Layer Instability over a Blunt Cone

Clifton H. Mortensen* and Xiaolin Zhong†
University of California, Los Angeles, Los Angeles, California 90049

DOI: 10.2514/1.J054404

There has been little research into surface-ablation effects on hypersonic boundary-layer instability, and the current understanding of real-gas effects on hypersonic boundary-layer instability still contains uncertainties. The objective of the current work was to analyze the hypersonic boundary-layer transition process using linear-stability theory, in which surface ablation, as well as real-gas effects, is present, and the second mode is the dominant instability mode. A thermochemical nonequilibrium linear-stability-theory code with a gas-phase model that includes multiple carbon species, as well as a linearized surface graphite-pseudoablation model, is developed and validated. It is validated with previously published linear-stability analysis and direct-numerical-simulation results. A high-order method for discretizing the linear-stability equations is used, which can easily include high-order boundary conditions. The developed linear-stability code, with mean-flow solutions produced from a high-order shock-fitting direct-numerical-simulation method for hypersonic flows with thermochemical nonequilibrium and surface-chemistry boundary conditions for graphite pseudoablation, is used to study hypersonic boundary-layer instability for a 7 deg half-angle blunt cone at Mach 15.99 and the Reentry-F experiment at 100 kft. Multiple mean-flow simulations are obtained with the same geometry and freestream conditions to help separate real-gas, blowing, and carbon-species effects on hypersonic boundary-layer instability. For the case at Mach 15.99, an *N* factor comparison shows that real-gas effects significantly destabilize the flow when compared to an ideal gas. Blowing is destabilizing for the real-gas simulation, and has a negligible effect for the ideal-gas simulation due to the different locations of instability onset. Notably, carbon species resulting from ablation are shown to slightly stabilize the flow for both cases. It is also found that ablating nose-cone effects may safely be excluded when determining the *N* factor at transition for Reentry-F at 100 kft.

Nomenclature

c_r	=	phase speed, m/s
c_s	=	mass fraction of species s
e	=	specific total energy, J/kg
e_v	=	specific vibration energy, J/kg
$e_{v,s}$	=	species specific vibration energy, J/kg
M_s	=	species molecular weight, kg/mol
$\dot{m}$	=	mass flux per area, kg/m^2 · s
$Q_{T-V,s}$	=	species vibration-energy transfer rate, J/m^3 · s
R	=	universal gas constant, 8.3143 J/mol · K
s	=	surface streamline, species
T	=	translation–rotation temperature, K
T_V	=	vibration temperature, K
u_j	=	velocity in jth direction, m/s
w	=	wall
α_r	=	wave number, 1/m
$-\alpha_i$	=	growth rate, 1/m
δ_{ij}	=	Kronecker delta
μ	=	viscosity, kg/m · s
ρ	=	density, kg/m^3
ϕ_Z	=	phase of Z, deg
ω_s	=	rate of species production, kg/m^3 · s
∞	=	freestream

Presented as Paper 2013-2981 at the 43rd AIAA Fluid Dynamics Conference, San Diego, CA, 24–27 June 2013; received 16 April 2015; revision received 21 July 2015; accepted for publication 27 July 2015; published online 12 January 2016.

*Graduate Student, Mechanical and Aerospace Engineering; clifton.mortensen@engineering.ucla.edu. Student Member AIAA.

†Professor, Mechanical and Aerospace Engineering; xiaolin@seas.ucla.edu. Associate Fellow AIAA.

I. Introduction

THERMAL protection systems (TPSs) are commonly used to protect hypersonic vehicles from the harsh, high-enthalpy environment they operate in [1]. Often, a TPS is ablating, such as those made using graphite or phenolic impregnated carbon ablator (PICA). Examples include nose cones or fins for thermal protection of hypersonic vehicles, such as the nose cone for the Reentry-F flight vehicle [2,3]. The flight of the Reentry-F vehicle is important to the hypersonic-transition community, as actual in-flight measurements of transition data at high Mach numbers were obtained and are available for analysis. Hypersonic free-flight transition measurements are not common and are highly valuable for understanding actual in-flight transition. Some of the free-flight transition data available for cones have ablating nose cones, such as the Reentry-F and Sherman and Nakamura [4] cases. Therefore, to gain the most insight from these valuable measurements, it is important to understand to what degree the ablating nose cone affects the transition location.

The a priori identification of the location of boundary-layer transition for hypersonic vehicles at given flight conditions has proven difficult. However, for a low-disturbance environment, it is commonly understood that, for flat plates and straight cones, the amplification of linear wavelike disturbances, such as the second mode for hypersonic flows, can lead to parametric instabilities and mode interactions, and then to breakdown and finally turbulence. The eigenmode growth of linear wavelike disturbances provides initial conditions to nonlinear breakdown, and the most unstable frequencies persist downstream. This makes the eigenmode-growth region essential to understanding hypersonic boundary-layer transition. Common methods for modeling these linear wavelike disturbances are linear-stability theory (LST), parabolized stability equations (PSEs), and direct numerical simulation (DNS). These methods are designed to predict the growth or decay of wavelike disturbances based on a laminar mean-flow profile. Here, LST is used to study real-gas effects and ablation-induced outgassing effects on hypersonic boundary-layer instability over a blunt cone.

During the process of ablation, the surface material is removed to reduce the energy transferred from the flow to the vehicle. Material

removal from the surface causes surface recession, which may not be constant over the length of the surface due to varying surface temperatures and pressures. For the cases simulated here, $c_r \gg \dot{S}_{\max}$, in which $\dot{S}_{\max}$ is the maximum surface-recession rate. Because the phase velocity of the second-mode instability is much larger than the surface-recession rate, it is likely that the effect of surface recession on modal instability for the tested cases is small. Material removal may also cause a significant roughening of the surface. This roughening may significantly alter the transition process, such as leading to bypass transition, in which eigenmode growth is completely bypassed. Currently, there is substantial uncertainty concerning the effects of surface roughness on hypersonic boundary-layer transition. In [5], the effects of roughness on hypersonic boundary-layer transition are reviewed, in which it is noted that the characterization of ablation-induced surface roughness in flight has significant uncertainty. Also, it is noted that an understanding of the instabilities that lead to transition for a smooth wall is needed to understand the experimental results of roughened surfaces. With this in mind, this research will use a simplified pseudoablation approach, in which surface recession and roughness are neglected to provide a more tractable problem, and hopefully increase the understanding of ablation on boundary-layer instability.

Significant research on the linear stability of boundary layers has been performed by Mack [6]. Mack found that the major instability waves for hypersonic boundary layers with a perfect-gas assumption are the first and second modes. The following researchers have implemented numerical codes based on LST to compute the most unstable frequencies for a variety of flow conditions and gas models. Malik [7] implemented multiple numerical methods for the linear stability of perfect-gas boundary-layer flows. Most research on hypersonic boundary-layer stability has used a perfect-gas model, and few researchers have studied the effects of thermochemical nonequilibrium. Chang et al. [8] comment on real-gas effects, stating that it is "very important to account for the chemistry effect in future transition prediction for hypersonic vehicles." Stuckert and Reed [9], Hudson et al. [10], Hudson [11], Chang et al. [8], and Johnson et al. [12] studied boundary-layer stability in nonequilibrium chemically reacting hypersonic boundary layers using LST. It was found that dissociation of air species is destabilizing to the second mode and stabilizing to the first mode. Ma and Zhong [13] studied the receptivity of freestream disturbances using DNS for a Mach 10 nonequilibrium oxygen flow over a flat plate. They found that, in a Mach 10 oxygen flow, there is a significant real-gas destabilizing effect on the second-mode waves. Malik [14] and Johnson and Candler [15] showed that LST and PSE, including real-gas effects, can be used to estimate transition onset in hypersonic free flight.

Currently, there has been a limited amount of numerical research on how ablation and surface-chemistry models effect hypersonic boundary-layer receptivity and instability. Johnson et al. [16] used linear-stability analysis to analyze nonreacting and reacting hypersonic boundary-layer stability with blowing and suction. Li et al. [17] studied boundary-layer instability mechanisms for hypersonic perfect-gas flows over slender cones and blunt capsules at zero angle of attack and an angle of attack of 16 deg. They found that, for the slender cone, outgassing is moderately stabilizing to the second mode, and for the blunt capsule, outgassing is destabilizing to the first mode.

A deficiency of previous research is that blowing profiles have been rather artificial, that is, they are set from a similarity solution or at random. This can make the tested blowing profiles quite different than realistic blowing profiles. Also, other effects due to surface ablation, such as injection of surface species into the mean flow, have been neglected. The current work seeks to remedy these deficiencies by using a realistic blowing profile computed from a surface-chemistry model and by blowing a realistic gas composition computed from a surface-chemistry model, rather than simply blowing air.

This paper is an extension of previous research described in [18], in which a thermochemical nonequilibrium DNS code with boundary conditions to approximate graphite ablation was validated and unsteady findings were presented. Unsteady DNS results showed that a real-gas simulation with surface ablation was significantly destabilized compared to a perfect-gas simulation with and without surface blowing. However, the causes of the increased instability were not separated, that is, real-gas, blowing, and carbon-species effects were not separated. In this research, the effects will be separated and quantified.

The goal of this paper was twofold: 1) to develop and validate a linearized surface model for graphite pseudoablation, which is included into our new thermochemical nonequilibrium linear-stability solver; and 2) to study real-gas effects, blowing effects, and carbon-species effects on hypersonic boundary-layer instability over a blunt cone using the developed linear-stability-theory code. A thermochemical nonequilibrium linear-stability-theory code is required to help analyze boundary-layer waves, such as identifying the fast and slow modes, as well as quickly identifying unstable frequency ranges. A linearized surface model for graphite pseudoablation is required in the LST code to accurately compare to DNSs of graphite ablation and to account for surface phenomena due to ablation. Mortensen and Zhong [18] give the DNSs for the ablative mean flow and ideal-gas mean flows. A simplified approach to ablation prediction is used to help keep the research focus on hypersonic boundary-layer instability. An 11-species gas model is used to model chemical nonequilibrium. It contains a standard five-species-air model (N_2, O_2, NO, N, and O). The remaining species contain carbon (C_3, CO_2, C_2, CO, CN, and C), and are obtained from sublimation, oxidation, and ablation product reactions. A two-temperature model is used to simulate thermal nonequilibrium. Only graphite ablation is considered without the effects of surface recession and ablation-induced roughness. The surface reactions considered contain oxidation, recombination of atomic oxygen, and sublimation. A surface mass balance is used to set species mass fractions at the surface. Although current TPS materials have advanced beyond graphite, many are still carbon based. For example, Chen and Milos [19] use the same surface reactions to model graphite and PICA with the addition of pyrolysis gas injection for PICA. Thus, graphite ablation provides a good starting point for understanding how carbonaceous ablation-induced outgassing affects boundary-layer instability.

The paper is organized as follows: it will start with an overview of the governing equations and the gas-phase models, followed by the numerical method for the LST code. An overview of the surface-chemistry model as well as the linearized surface-chemistry model will then be given. After which, the LST code with the linearized surface model for graphite pseudoablation will be validated with previously published results from [11] and unsteady data from the DNS code, which were previously validated in [18]. After validation, the instability characteristics of a 7 deg half-angle blunt cone at Mach 15.99 will be computed to assess the real-gas effects, blowing effects, and carbon-species effects on hypersonic boundary-layer instability. Then, the in-flight transition measurements of the Reentry-F flight experiment at 100 kft are examined, including and excluding surface ablation.

II. Governing Equations and Gas-Phase Models

The governing equations are formulated for a thermochemical nonequilibrium flow using a two-temperature model. The two temperatures are used to represent translation–rotation energy and vibration energy. The translational and rotational energy modes are assumed to be in equilibrium, and the rotational energy mode is assumed to be fully excited. Eleven nonionizing species with finite rate chemistry are used, in which the 11-species model (N_2, O_2, NO, C_3, CO_2, C_2, CO, CN, N, O, and C) is used to simulate air, surface reactions, and reactions of air with ablation products. The conservative three-dimensional Navier–Stokes equations consist of 11-species mass-conservation equations, three momentum-conservation equations, the vibration-energy-conservation equation, and the total-energy-conservation equation. Mortensen and Zhong [18], Wang and Zhong [20], and Prakash et al. [21] have used similar formulations for simulating thermochemical nonequilibrium flow. For both the mean-flow and LST formulations, the governing

equations as well as the gas-phase models are the same. Written in vector form, the governing equations are

$$\frac{\partial \boldsymbol{U}}{\partial t} + \frac{\partial F_j}{\partial x_j} + \frac{\partial G_j}{\partial x_j} = W \tag{1}$$

in which $\boldsymbol{U}$ is the state vector of conserved quantities, and W is the source term defined by

$$\boldsymbol{U} = \begin{bmatrix} \rho_1 \\ \vdots \\ \rho_{\text{ns}} \\ \rho u_1 \\ \rho u_2 \\ \rho u_3 \\ \rho e \\ \rho e_v \end{bmatrix}, \qquad W = \begin{bmatrix} \omega_1 \\ \vdots \\ \omega_{\text{ns}} \\ 0 \\ 0 \\ 0 \\ 0 \\ \sum_{s=1}^{\text{nms}} (Q_{T-V,s} + \omega_s e_{v,s}) \end{bmatrix}$$

in which ns denotes number of species, and nms is number of molecular species.

The inviscid and viscous fluxes are, respectively, F_j and G_j, and are defined by

$$F_j = \begin{bmatrix} \rho_1 u_j \\ \vdots \\ \rho_{\text{ns}} u_j \\ \rho u_1 u_j + p\delta_{1j} \\ \rho u_2 u_j + p\delta_{2j} \\ \rho u_3 u_j + p\delta_{3j} \\ (\rho e + p) u_j \\ \rho e_v u_j \end{bmatrix},$$

$$G_j = \begin{bmatrix} \rho_1 v_{1j} \\ \vdots \\ \rho_{\text{ns}} v_{\text{ns}j} \\ \tau_{1j} \\ \tau_{2j} \\ \tau_{3j} \\ -u_i \tau_{ij} - k_T \frac{\partial T}{\partial x_j} - k_V \frac{\partial T_V}{\partial x_j} + \sum_{s=1}^{\text{nms}} \rho_s h_s v_{sj} \\ -k_V \frac{\partial T_V}{\partial x_j} + \sum_{s=1}^{\text{nms}} \rho_s e_{v,s} v_{sj} \end{bmatrix}$$

in which $v_{sj} = -(1/c_s) D_s (\partial c_s / \partial x_j)$ is the species diffusion velocity, and $\tau_{ij} = \mu(\partial u_i/\partial x_j + \partial u_j/\partial x_i) - (2/3)\mu(\partial u_k/\partial x_k)\delta_{ij}$ is the viscous stress. The total energy per unit volume is defined by

$$\rho e = \sum_{s=1}^{\text{ns}} \rho_s c_{v,s} T + \rho e_v + \frac{1}{2}\rho(u_1^2 + u_2^2 + u_3^2) + \sum_{s=1}^{\text{ns}} \rho_s h_s^o \tag{2}$$

in which h_s^o is the heat of formation of species s, and $c_{v,s}$ is the species translation–rotation specific heat at constant volume defined as

$$c_{v,s} = \begin{cases} \frac{5}{2}\frac{R}{M_s}, & s = 1, 2, \ldots, \text{nms} \\ \frac{3}{2}\frac{R}{M_s}, & s = \text{nms}+1, \ldots, \text{ns} \end{cases} \tag{3}$$

The vibration energy per unit volume is defined as

$$\rho e_v = \sum_{s=1}^{\text{nms}} \rho_s e_{v,s} = \sum_{s=1}^{\text{nms}} \rho_s \left(\sum_{m=1}^{\text{nmod}} \frac{g_{s,m} R}{M_s} \frac{\theta_{v,s,m}}{\exp(\theta_{v,s,m}/T_V) - 1} \right) \tag{4}$$

in which nmod refers to the number of vibrational modes for each polyatomic molecule, $\theta_{v,s,m}$ refers to the characteristic temperature of each vibrational mode, and $g_{s,m}$ is the degeneracy of each vibrational mode. For the diatomic species, there is only one vibrational mode, and the degeneracy is unity. For C_3 and CO_2, there are three vibrational modes, in which two modes have a degeneracy of unity and one has a degeneracy of two. The characteristic vibration temperatures and their degeneracies were taken from Park [22] for N_2, O_2, and NO, from Dolton et al. [23] for C_3, and from McBride et al. [24] for CO_2, C_2, CO, and CN.

To model chemical nonequilibrium, eight dissociation reactions and 16 exchange reactions are used. Each reaction is governed by a forward and backward reaction rate. The forward reaction rates and constants are obtained from Park [25], Bhutta and Lewis [26], and Park et al. [27]. The backward rate is computed from the forward rate and the equilibrium coefficient. The equilibrium coefficient is computed in two different ways. First, a curve fit from Park [22] is used. Second, the Gibbs-free-energy approach is used, in which curve fits to the Gibbs free energy are obtained from McBride et al. [24].

To calculate the source term in the vibration-energy equation representing the exchange of energy between the translation–rotation and vibration energies, the Landau–Teller formulation is used:

$$Q_{T-V,s} = \rho_s \frac{e_{v,s}(T) - e_{v,s}(T_V)}{< \tau_s > + \tau_{cs}} \tag{5}$$

in which $< \tau_s >$ is the Landau–Teller vibrational relaxation time given by Lee [28]. The term τ_{cs} is from Park [22] to more accurately model the relaxation time in areas of high temperatures occurring just downstream of the bow shock.

The viscosity of each species is computed using a Blottner curve fit. The coefficients are obtained from Blottner et al. [29], Gupta et al. [30], and Candler [31]. The mixture viscosity is then found using each species viscosity from a mixing rule obtained from Wilke [32]. The total heat conductivities for each energy mode are computed in a similar fashion as viscosity. The diffusion velocity is calculated using Fick's law and a constant Schmidt number of 0.5.

III. Surface-Chemistry Model

A surface-chemistry model is required to couple the ablating graphitic surface with the flow. The surface-chemistry model accounts for reactions occurring at the graphite surface between the solid surface carbon and freestream gaseous species. Six surface reactions are taken into account: the first two reactions allow for surface removal of material through oxidation; the third reaction accounts for surface recombination of atomic oxygen; and the last three are due to sublimation of C, C_2, and C_3. C_3 is commonly included in most graphite-ablation models, as sublimation of graphite produces mostly C_3 with smaller amounts of C, C_2, and heavier carbon species.

Nitridation is not included here, as there is still significant uncertainty in the nitridation coefficient. There has been recent experimental work to determine the nitridation coefficient in [33,34]. Likely, the nitridation coefficient is small, leading to a minimal impact on the simulation when nitridation is excluded. Recent results have also shown that the nitrogen-atom recombination reaction occurring at the surface of hot graphite is very fast [35,36]. For the tested cases, the nitrogen-atom concentration at the surface is only significant near the stagnation point, which is away from the flow instability studied. However, it would likely need to be included when studying instabilities when the mean flow had a high concentration of atomic nitrogen near the surface.

The reactions and reaction probabilities for oxidation and recombination of atomic oxygen are obtained from Park [37], yielding

$$(\text{C}) + \text{O}_2 \rightarrow \text{CO} + \text{O} \tag{6}$$

$$(\text{C}) + \text{O} \rightarrow \text{CO} \tag{7}$$

$$(C) + O + O \rightarrow (C) + O_2 \tag{8}$$

The oxidation rates are based on kinetic theory giving

$$k_m = \alpha_m \sqrt{\frac{RT_w}{2\pi M_s}} \tag{9}$$

in which α_m is the reaction probability for each reaction in Eqs. (6–8), respectively. The reaction probabilities are obtained experimentally yielding

$$\alpha_1 = \frac{1.43 \times 10^{-3} + 0.01 \exp(-1450/T_w)}{1 + 2 \times 10^{-4} \exp(13,000/T_w)} \tag{10}$$

$$\alpha_2 = 0.63 \exp(-1160/T_w) \tag{11}$$

$$\alpha_3 = 0.63 \exp(-1160/T_w) \tag{12}$$

From which, the associated surface-species mass flux may be found from

$$\dot{m}_{O_2} = -\rho_{O_2} k_1 + \rho_O k_3 \tag{13}$$

$$\dot{m}_{CO} = \frac{M_{CO}}{M_{O_2}} \rho_{O_2} k_1 + \frac{M_{CO}}{M_O} \rho_O k_2 \tag{14}$$

$$\dot{m}_O = \frac{M_O}{M_{O_2}} \rho_{O_2} k_1 - \rho_O k_2 - \rho_O k_3 \tag{15}$$

There are three reactions for sublimation

$$(C) \rightarrow C \tag{16}$$

$$(C) \rightarrow C_2 \tag{17}$$

$$(C) \rightarrow C_3 \tag{18}$$

and for each reaction, the mass flux is obtained from the Knudsen–Langmuir equation [38]

$$\dot{m}_s = \alpha_s (p_{v,s} - p_s) \sqrt{\frac{M_s}{2\pi R T_w}} \tag{19}$$

in which α_s is experimentally determined [39] for each carbon species. The vapor pressure of the three carbon species is given by

$$p_{v,s} = \exp\left(\frac{P_s}{T_w} + Q_s\right) p \text{ in atm} \tag{20}$$

in which P_s and Q_s are from [23].

Boundary conditions are needed to couple the surface-chemistry model with the gas model, as well as set wall conditions for both temperatures and pressure. At the surface, a surface energy balance is solved to find the temperature, and a surface mass balance is solved to find the mass fraction of each species. A simplified surface energy balance is used to avoid a complicated flow/solid coupling, and allowing the focus to stay on boundary-layer instability. The surface energy balance is

$$k_T \frac{\partial T}{\partial n} + k_V \frac{\partial T_V}{\partial n} + \sum_{s=1}^{ns} \rho h_s D_s \frac{\partial c_s}{\partial n} = \sigma \epsilon T^4 + \dot{m} \sum_{s=1}^{ns} c_s h_{s,o} \tag{21}$$

in which

$$h_{s,o} = \left(c_{v,s} + \frac{R}{M_s}\right) T + e_{v,s} + h_s^o + \frac{1}{2}(u_1^2 + u_2^2 + u_3^2) \tag{22}$$

and all values are defined at the wall. The constant $\epsilon = 0.9$ for the carbon surface and σ is the Stefan–Boltzmann constant. Each derivative is taken normal to the surface, in which n represents the direction normal to the surface.

The surface mass balance for each species is

$$\rho_s u_n - \rho D_s \frac{\partial c_s}{\partial n} = \dot{m}_s \tag{23}$$

in which u_n is the wall-normal velocity, and each value or derivative is taken at the wall. The total mass balance found from summing Eq. (23) is

$$\rho u_n = \dot{m} \tag{24}$$

in which the total mass flux is found from the sum of each species mass flux as

$$\dot{m} = \sum_{s=1}^{ns} \dot{m}_s \tag{25}$$

Lastly, a condition for pressure is required at the surface. It is common to assume that $\partial p/\partial n = 0$ from the wall-normal momentum equation for a wall with no slip. A finite velocity is obtained normal to the surface due to surface chemical reactions making $\partial p/\partial n = 0$ invalid. In the present work, fifth-order pressure extrapolation employing Lagrange polynomials is used, which allows the interior points to set the wall pressure.

IV. High-Order LST Numerical Method

Once mean-flow solutions have been obtained from a suitable mean-flow solver, such as the one given in [18], it is possible to analyze flow instability using linear-stability analysis. For the linear-stability analysis, a body-fitted orthogonal curvilinear coordinate system is used for axisymmetric bodies, in which x is in the streamwise direction, y is in the wall-normal direction, z is in the transverse direction, and the origin is located on the body surface. Curvature in the streamwise and transverse directions is included similar to [40]. Elemental lengths are defined as $h_1 dx$, dy, and $h_3 dz$, in which

$$h_1 = 1 + \kappa y \tag{26}$$

$$h_3 = r_b + y \cos(\theta) \tag{27}$$

and in which κ is the streamwise curvature, r_b is the local radius of the body, and θ is the local half-angle of the body. The coordinate system for a flat plate is recovered by setting h_1 and h_3 to unity. For a straight cone, only h_3 is required and h_1 is set to unity.

The derivation of the thermochemical nonequilibrium LST equations follows the work of [11] excepting the species-velocity terms, which are substituted into the governing equations before linearization similar to [41]. The LST equations are derived from the nonconservative form of the governing equations, in which the instantaneous flow is composed of a mean and fluctuating component $q = \bar{q} + q'$. Here, q represents any flow variable, such as velocity,

density, temperature, etc. The instantaneous flow is then substituted into the governing equations, in which the steady flow is assumed to satisfy the governing equations and is subtracted out. The mean flow is assumed to be a function of the wall-normal coordinate y only [i.e., $\bar{q}(x, y, z) \approx \bar{q}(y)$], and the flow disturbances are assumed to be small (i.e., linear). The perturbations are then assumed to be in the form of a normal mode described by

$$q'(x, y, z) = \hat{q}(y) \exp[i(\alpha x + \beta z - \omega t)] \tag{28}$$

in which ω is the circular frequency of the mode, and α and β are the wave numbers. Commonly, ω and β are assumed to be real, and the wave number α is assumed to be complex, which means the modes grow in space rather than time. If ω is complex and α and β are real, then the modes grow in time rather than space. For comparison to DNS, the spatial-stability approach is used, that is, α is complex, which results in the dispersion relation $\alpha = \Omega(\omega, \beta)$. Substituting in the normal-mode form for the perturbations reduces the problem to a coupled set of ns + 5 ordinary differential equations:

$$\left(\boldsymbol{A}\frac{d^2}{dy^2} + \boldsymbol{B}\frac{d}{dy} + \boldsymbol{C}\right)\boldsymbol{\phi} = \boldsymbol{0} \tag{29}$$

in which $\boldsymbol{\phi} = \{\hat{\rho}_1, \hat{\rho}_2, \ldots, \hat{\rho}_{\text{ns}}, \hat{u}, \hat{v}, \hat{w}, \hat{T}, \hat{T}_V\}^T$, and $\boldsymbol{A}$, $\boldsymbol{B}$, and $\boldsymbol{C}$ are complex square matrices of size ns + 5. This is now a boundary-value problem, in which the derivative operators can be discretized and the equations solved numerically.

For hypersonic compressible boundary layers, it is important to have high grid resolution near the generalized inflection point [6]. The current computational grid is used to cluster grid points around the inflection point, and has been used by previous researchers [10]. It is defined so

$$y = \frac{a\eta}{b - \eta} \tag{30}$$

in which

$$a = \frac{y_{\max} y_i}{(y_{\max} - 2y_i)} \tag{31}$$

$$b = 1 + \frac{a}{y_{\max}} \tag{32}$$

and $y_{\max}$ is the outer domain boundary, y_i is the location of the generalized inflection point, and η runs from zero to one. For hypersonic boundary layers, the generalized inflection point moves toward the boundary-layer edge, and so y_i may be placed near the boundary-layer edge. If grid metrics are required, they can be computed directly from Eq. (30).

With the grid defined, it is now possible to discretize the derivative operators. In [7], there is an excellent overview of numerical methods suitable for stability calculations of hypersonic flows, which include finite difference, compact difference, and spectral formulations. A fourth-order central-difference scheme has been used by previous researchers [11,42] to good effect. Here, a different approach than what has previously been used for hypersonic stability calculations is taken. The first- and second-derivative operators in the wall-normal direction are discretized by taking derivatives of Lagrange polynomials in physical space. If x_p is the grid point, in which a first derivative is required, then

$$\left.\frac{\partial f}{\partial x}\right|_{x_p} = \sum_{i=1}^{N} A_i f_i \tag{33}$$

in which

$$A_i = \frac{\sum_{\substack{j=1 \\ j\neq i}}^{N} \prod_{\substack{k=1 \\ k\neq i \\ k\neq j}}^{N} (x_p - x_k)}{\prod_{\substack{m=1 \\ m\neq i}}^{N} (x_i - x_m)} \tag{34}$$

and N is the total number of points in the stencil. Similarly, for a second derivative at x_p

$$\left.\frac{\partial^2 f}{\partial x^2}\right|_{x_p} = \sum_{i=1}^{N} B_i f_i \tag{35}$$

in which

$$B_i = \frac{\sum_{\substack{\ell=1 \\ \ell\neq i}}^{N} \sum_{\substack{j=1 \\ j\neq i \\ j\neq \ell}}^{N} \prod_{\substack{k=1 \\ k\neq i \\ k\neq j \\ k\neq \ell}}^{N} (x_p - x_k)}{\prod_{\substack{m=1 \\ m\neq i}}^{N} (x_i - x_m)} \tag{36}$$

For the interior points, a centered stencil is used, thus requiring an odd number of points. An even number of points may be used, which would require an offset stencil. For grid points near the boundary, an offset stencil is used, in which the number of points in the stencil is maintained. It should be noted that the largest source of numerical error from approximating the derivatives in this fashion will come from the second-derivative approximation. To decrease this error, more points may be used in the second-derivative stencil than in the first-derivative stencil, but here, an equal number of points are used for each derivative approximation. These derivative operators are applied in physical space rather than computational space to avoid Runge's phenomena, in which spurious oscillations can occur for a one-sided stencil with a high order of approximation. Also, in areas of low grid density, this method is susceptible to odd–even decoupling of the solution. If the derivative operators of Eqs. (33) and (35) are applied to a centered stencil in computational space, the standard central finite difference coefficients are obtained. In other words, the fourth-order method used by previous researchers for interior points can be obtained from the current method using a five-point stencil in computational space.

There are a couple advantages to approximating the derivatives in this fashion. Once the subroutines for computing the coefficients are set up, it is trivial to change the number of points used to approximate the derivatives. This makes it easy to switch from low to high order or vice versa, without making any changes to the code, as the order of the method is dependent upon the number of points chosen for the derivative stencils. Because the derivatives are taken in physical space rather than computational space, grid metrics are not required. Although it is not used here, this allows an arbitrary placement of grid points within the computational domain. Also, the formulation for derivatives at the boundary can use the same derivative approximations, which easily integrate high-order boundary conditions into the code. As one of the main focal points in the current work for developing a thermochemical nonequilibrium LST code is to include gas/surface interactions, wall-normal derivatives are quite important, making this technique a good fit.

After discretization, nonlinearities exist in α, and so the global method suggested in [7] is used to compute the eigenvalue spectrum with $\alpha^2 = 0$. This method computes the eigenvalues from a generalized eigenvalue problem $\tilde{\boldsymbol{A}}\boldsymbol{\phi} = \alpha\tilde{\boldsymbol{B}}\boldsymbol{\phi}$, in which the LAPACK [43] subroutine ZGGEV is used to obtain a solution. From the eigenvalue spectrum, an initial guess can be obtained for the local method, which results in $\bar{\boldsymbol{A}}\boldsymbol{\phi} = \bar{\boldsymbol{B}}$, and the eigenvalue is found iteratively without dropping the α^2 terms. The LAPACK subroutine ZGESV is used to solve the local problem. It is also possible to avoid the computationally intensive global method and obtain an initial guess for α from a nearby streamwise location, similar frequency, or a DNS, assuming the unsteady DNS results are available.

Boundary conditions are required in the freestream and at the wall for LST. In the freestream, all perturbations are zero except the wall-normal velocity perturbation, which is found from the mass-conservation equation similar to [44]. The freestream boundary conditions are set near $0.98H_s$, in which H_s is the height of the shock measured from the wall. It is possible to linearize the Rankine–Hugoniot jump conditions at the shock, which would be required for a mode with an eigenfunction that oscillates in the freestream, such as the unstable supersonic modes shown in [8]. However, the unstable second mode studied here has a decaying eigenfunction in the freestream, in which the current boundary conditions used are suitable.

The boundary conditions at the wall are slightly more complicated. There are ns + 5 independent variables in the stability calculations; therefore, ns + 5 conditions are required at the wall. The approach taken here is to linearize all of the equations used to set the wall boundary conditions in the mean-flow simulation. The linearization procedure is consistent with the linearization of the interior flow. Of these ns + 5 conditions, the simplest are the no slip in the wall-tangent directions resulting in $\hat{u}_1 = \hat{u}_3 = 0$. The surface energy balance in Eq. (21) can be linearized resulting in

$$\begin{aligned}
&\frac{dT}{dy}k' + k\frac{\partial T'}{\partial y} + \frac{dT_V}{dy}k'_V + k_V\frac{\partial T'_V}{\partial y} + \rho\sum_{s=1}^{\text{ns}} h_s D_s \frac{\partial c'_s}{\partial y} \\
&\quad + \rho\sum_{s=1}^{\text{ns}} h_s \frac{\partial c_s}{\partial y} D'_s + \rho\sum_{s=1}^{\text{ns}} D_s \frac{\partial c_s}{\partial y} h'_s \\
&\quad + \left(\sum_{s=1}^{\text{ns}} h_s D_s \frac{\partial c_s}{\partial y}\right)\rho' - 4\sigma\epsilon T^3 T' - \dot{m}\sum_{s=1}^{\text{ns}} c_s h'_{s,o} - \dot{m}\sum_{s=1}^{\text{ns}} h_{s,o} c'_s \\
&\quad - \left(\sum_{s=1}^{\text{ns}} c_s h_{s,o}\right)\dot{m}' = 0
\end{aligned} \tag{37}$$

in which the perturbation of the diffusion coefficients and the species mass-flux terms are dependent on the specific gas model and surface-chemistry model used. They can be found from a first-order Taylor series expansion. Note that the overbars have been dropped from the steady terms for simplicity, and y denotes the wall-normal coordinate. As there are ns + 5 independent variables, it is required to put Eq. (37) in terms of these independent variables. Then, the normal-mode form for the perturbations may be substituted for the equation to be suitable as a boundary condition. For the gas model and surface-chemistry model given here, this results in

$$\begin{aligned}
&\frac{dT}{dy}\left(\sum_{r=1}^{\text{ns}}\frac{\partial k}{\partial \rho_r}\hat{\rho}_r + \frac{\partial k}{\partial T}\hat{T}\right) + k\frac{\partial \hat{T}}{\partial y} + \frac{dT_V}{dy}\left(\sum_{r=1}^{\text{ns}}\frac{\partial k_V}{\partial \rho_r}\hat{\rho}_r + \frac{\partial k_V}{\partial T}\hat{T} + \frac{\partial k_V}{\partial T_V}\hat{T}_V\right) \\
&\quad + k_V\frac{\partial \hat{T}_V}{\partial y} + \rho\sum_{s=1}^{\text{ns}} h_s D_s \frac{\partial}{\partial y}\left(\frac{\hat{\rho}_s}{\rho} - \frac{c_s}{\rho}\sum_{r=1}^{\text{ns}}\hat{\rho}_r\right) \\
&\quad + \rho\sum_{s=1}^{\text{ns}} h_s \frac{\partial c_s}{\partial y}\left(\sum_{r=1}^{\text{ns}}\frac{\partial D_s}{\partial \rho_r}\hat{\rho}_r + \frac{\partial D_s}{\partial T}\hat{T}\right) \\
&\quad + \rho\sum_{s=1}^{\text{ns}} D_s \frac{\partial c_s}{\partial y}\left[\left(c_{v,s} + \frac{R}{M_s}\right)\hat{T} + \frac{\partial e_{v,s}}{\partial T_V}\hat{T}_V\right] \\
&\quad + \left(\sum_{s=1}^{\text{ns}} h_s D_s \frac{\partial c_s}{\partial y}\right)\sum_{r=1}^{\text{ns}}\hat{\rho}_r - 4\sigma\epsilon T^3\hat{T} \\
&\quad - \dot{m}\sum_{s=1}^{\text{ns}} c_s\left[\left(c_{v,s} + \frac{R}{M_s}\right)\hat{T} + \frac{\partial e_{v,s}}{\partial T_V}\hat{T}_V + \frac{\dot{m}}{\rho}\hat{v}\right] \\
&\quad - \frac{\dot{m}}{\rho}\sum_{s=1}^{\text{ns}} h_{s,o}\left(\hat{\rho}_s - c_s\sum_{r=1}^{\text{ns}}\hat{\rho}_r\right) \\
&\quad - \sum_{n=1}^{\text{ns}} c_n h_{n,o}\left[\sum_{r=1}^{\text{ns}}\sum_{s=1}^{\text{ns}}\frac{\partial \dot{m}_s}{\partial \rho_r}\hat{\rho}_r + \sum_{s=1}^{\text{ns}}\frac{\partial \dot{m}_s}{\partial T}\hat{T}\right] = 0
\end{aligned} \tag{38}$$

in which all values and derivatives are defined at the wall. To this point, the derivation of the linearized surface energy balance has made no assumptions about parallel flow, and so it is still applicable to nonparallel methods. Recall from Eq. (24) that $\dot{m} = \rho u_n$, which requires any terms containing $\dot{m}$ to be set to zero to enforce the parallel-flow assumption. Also, note that this equation is in essence imposing an upper bound on the temperature perturbation at the wall. Mack [6] notes that "for almost any frequency, it is not possible for the wall to do other than to remain at its mean temperature," which would require that $\hat{T} = 0$. For ablative flows, the exact boundary between the wall and the fluid is a little less sharp. There may be melting of the surface material and/or pyrolysis gas injection that are not present for a standard nonporous, wall-bounded flow. Taking these physical mechanisms into account, it is quite possible for $\hat{T} \neq 0$. In reality, $\hat{T}$ at the surface may lie between these two extremes, and so it is useful to see how each boundary condition influences instabilities. Both of these cases are tested in Sec. VI. For either case of temperature perturbation, the wall is assumed to be in thermal equilibrium, resulting in $\hat{T}_V = \hat{T}$.

Conditions on each species-density perturbation are required at the wall. Equation (23) gives the condition on the species density at the wall for the mean-flow simulation. A linearization of this equation yields

$$\begin{aligned}
&\rho_s v' + \frac{\dot{m}}{\rho}\rho'_s - \rho D_s \frac{\partial}{\partial y}\left(\frac{\rho'_s}{\rho} - \frac{c_s}{\rho}\sum_{r=1}^{\text{ns}}\rho'_r\right) - \rho\frac{\partial c_s}{\partial y}D'_s \\
&\quad - D_s\frac{\partial c_s}{\partial y}\sum_{r=1}^{\text{ns}}\rho'_r - \dot{m}'_s = 0
\end{aligned} \tag{39}$$

in which, once again, the overbars denoting steady conditions have been dropped for simplicity, and $\dot{m}'_s$ is the species mass-flux perturbation related to the specific gas/surface interaction model. Substituting in the normal mode for each independent perturbation gives ns wall conditions in the form

$$\begin{aligned}
&\rho_s\hat{v} + \frac{\dot{m}}{\rho}\hat{\rho}_s - \rho D_s\frac{\partial}{\partial y}\left(\frac{\hat{\rho}_s}{\rho} - \frac{c_s}{\rho}\sum_{r=1}^{ns}\hat{\rho}_r\right) \\
&\quad - \rho\frac{\partial c_s}{\partial y}\left(\sum_{r=1}^{\text{ns}}\frac{\partial D_s}{\partial \rho_r}\hat{\rho}_r + \frac{\partial D_s}{\partial T}\hat{T}\right) - D_s\frac{\partial c_s}{\partial y}\sum_{r=1}^{\text{ns}}\hat{\rho}_r \\
&\quad - \sum_{r=1}^{\text{ns}}\frac{\partial \dot{m}_s}{\partial \rho_r}\hat{\rho}_r - \frac{\partial \dot{m}_s}{\partial T}\hat{T} = 0
\end{aligned} \tag{40}$$

Once again, note that the parallel-flow assumption has not been made yet. To make the parallel-flow assumption, simply drop the terms with $\dot{m}$. Note that the equation can be further simplified if $\hat{T} = 0$ by dropping all $\hat{T}$ terms.

With the species surface mass balance linearized, recall that a total mass balance was used to set the wall-normal velocity [Eq. (24)] in the mean-flow simulation. Further recall that this condition is found from a linear combination for each species surface mass balance. Therefore, a linearization of this equation will result in no new information at the boundary. For the boundary to be adequately constrained, another equation is required. In the mean-flow simulation, pressure extrapolation is used to account for the incoming characteristic at the wall. Linearizing the pressure-extrapolation condition and substituting in the normal modes result in

$$\begin{aligned}
&\left(\sum_{s=1}^{\text{ns}}\rho_s\frac{R}{M_s}\hat{T}\right)_1 + \left(\sum_{s=1}^{\text{ns}}\frac{R}{M_s}T\hat{\rho}_s\right)_1 \\
&\quad - \sum_{j=2}^{N}\gamma_j\left(\sum_{s=1}^{\text{ns}}\rho_s\frac{R}{M_s}\hat{T} + \sum_{s=1}^{\text{ns}}\frac{R}{M_s}T\hat{\rho}_s\right)_j = 0
\end{aligned} \tag{41}$$

in which the subscript 1 denotes the grid point at the wall, N is the number of points used, and γ_j are the weights for extrapolation. This accounts for the last required boundary condition and is used in place

of a $\hat{v}$ equation. It is also possible to linearize the total mass-flux equation and substitute the linearized pressure-extrapolation condition for one of the linearized surface-mass-balance equations. Both methods were tested, and the differences between the two were negligible.

V. LST Validation

To validate the LST code with the full linearized-surface-model boundary conditions, a comparison is given of the results from the LST code and the results from a DNS [18].

A. Grid-Convergence Study

Before a code comparison can be performed to DNS results, a grid-convergence study must be done to determine the required number of grid points for the LST grid. Three different grid densities were used with 100, 200, and 300 points, respectively. A comparison for the amplification rate at multiple frequencies is given in Fig. 1. For the 200-grid-point solution, the percent relative error for the amplification rate is less than 1% for the majority of the unstable frequency range. The error increases near the edges of the frequency range because the amplification rate is near zero. Two hundred grid points yield a grid-converged solution for this streamwise location.

B. LST Comparison to DNS

In the shock-fitting DNS, the shock is treated as a computational boundary using the Rankine–Hugoniot jump conditions. Once a mean-flow simulation has converged, fast acoustic waves in the freestream are continuously imposed on the bow shock, and their behavior is simulated as they pass through the entire domain. This approach does not simulate the behavior of a single mode like LST, but rather multiple modes can be present for each frequency. For the most consistent comparison, a streamwise location was selected where DNS results showed a clean exponential disturbance growth (i.e., no modulation). This was done because exponential growth is indicative of modal growth, and therefore, a dominant boundary-layer mode, rather than multiple competing modes. The streamwise location selected is s = 0.564 m measured along the cone surface from the stagnation point.

Figure 2 gives a comparison between DNS and LST of the amplitude and phase for a second-mode wave ($\beta = 0$) at a frequency of 525 kHz and a streamwise distance $s = 0.564$ m. The LST eigenfunctions were computed using a fourth-order stencil. For both temperatures, the comparison is quite good. Both the temperature and its gradient and phase near the wall compare well. The linearized surface energy equation, which is used in conjunction with the other boundary conditions to set the translation–rotation temperature at the wall, accurately compares with the DNS results. Similarly, each density perturbation and its near-wall gradient and phase compare well with the DNS results near the wall, showing that the linearized surface mass balances are implemented correctly. At this streamwise location in the DNS, there is a wave that has crossed the bow shock due to the fast acoustic forcing in the freestream and is approaching the edge of the boundary layer ($y = 3.15 \times 10^{-3}$ m). This wave is not modal and is likely composed of multiple waves in the continuous spectra. This causes some oscillatory behavior near the boundary-layer edge that is seen in the DNS, but is not due to the second mode. Therefore, differences between the two simulation methods in the amplitude and phase near the boundary-layer edge are most likely caused from this incoming wave.

Overall, the comparison between these two significantly different methods is good. The eigenfunction obtained from LST accurately compares to DNS for the amplitude and phase of the individual flow variables. The comparison inside the boundary layer, where the second mode is dominant, is good.

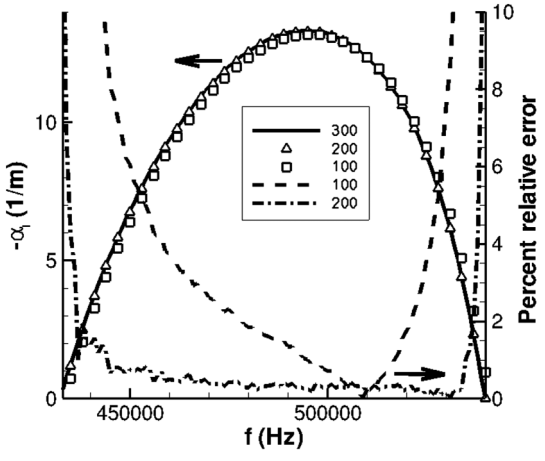

Fig. 1 Comparison of streamwise velocity.

C. Order-of-Error Estimate

As the derivative operators used to solve Eq. (29) are implemented in a nonstandard fashion, an order-of-error estimate is given to show the approximate order of the error incurred. Three different schemes were tested. Schemes 1 and 2 use the approach described in Sec. IV with a three-point and five-point stencil, respectively. In the previous research of Mortensen and Zhong [45], a fourth-order central approximation was used for interior derivatives, a second-order central approximation was used one point away from the boundary, and a first-order approximation was used at the boundaries. Each of these was taken using the standard centered finite difference stencil in computational space similar to [11]. This will be called scheme 3.

Figure 3 shows a plot of the error in the growth rate for the three schemes. The dashed lines represent ideal second- and fourth-order convergence rates useful for comparison. Scheme 1 has a convergence rate of 1.87, which is to be expected for a consistently three-point stencil. Scheme 2 has a convergence rate of 3.98, which is also expected for a consistently five-point stencil. Scheme 3 has a convergence rate of 2.39, which is lower than fourth order due to the lower-order stencils used near the boundary. Of the schemes tested, the scheme that uses a consistently five-point stencil, rather than switching to first order on the boundaries, gives the method with the rate of convergence nearest to four. The high-order numerical method proposed in Sec. IV has rates of convergence consistent with the number of points used in the derivative stencil.

VI. Linear-Stability Analysis of $M_\infty = 15.99$ Blunt Cone

LST is able to predict instability waves and their corresponding growth rates from steady boundary-layer profiles. The characteristics of an instability wave are strongly tied to the mean-flow boundary-layer profile, which is taken as an input for the linear-stability analysis. It is possible to use a single mean-flow boundary-layer profile computed using one gas model, and then change gas models in an LST code to predict how the characteristics of only instability waves will behave with changing models. This has been done to good effect by previous researchers [12]. Because instability waves are tied so strongly to the mean-flow profiles, to predict how different gas types (i.e., ideal gas and real gas) effect the entire process of hypersonic boundary-layer transition, the mean flow as well as the computation of instability waves needs to be performed with each of the separate models. Similarly, both a mean flow and instability waves need to be computed to assess the overall effect of surface chemistry, such as wall catalycity and surface ablation, on hypersonic boundary-layer instability. By computing a mean flow and the corresponding instability waves with the different models, an accurate comparison of the gas effects on flow instability, rather than simply the instability waves, can be given.

A. Steady-State Solutions of $M_\infty = 15.99$ Blunt Cone

In this research, one of the goals is to assess real-gas effects and ablation effects, which are in the form of surface chemistry, on

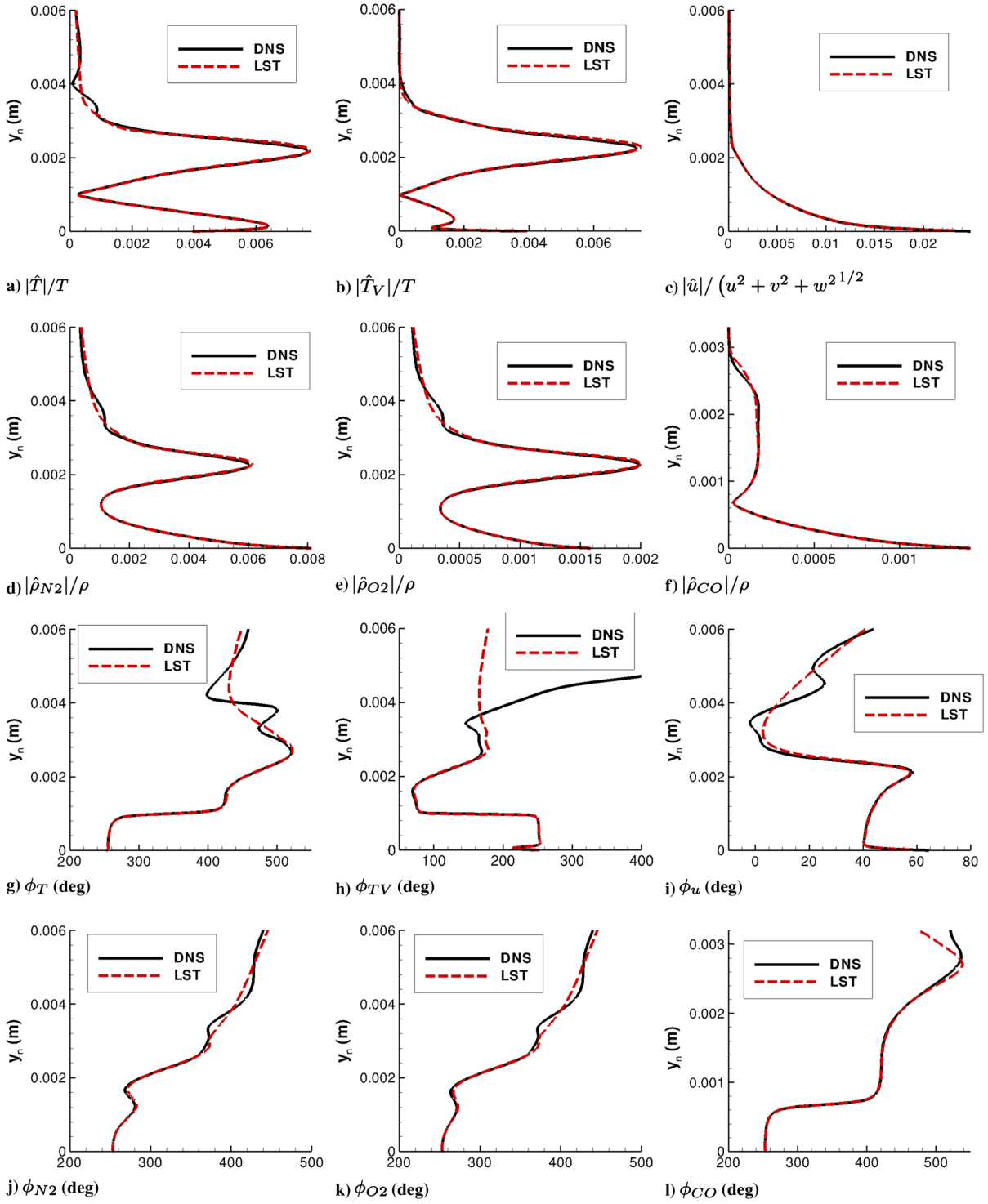

Fig. 2 Eigenfunction amplitude and phase comparison between DNS and LST for select variables.

hypersonic boundary-layer instability. To do this, five distinct steady simulations were run. Each of these steady simulations has the same geometry and the same freestream conditions. The geometry for each case is a sphere cone with a nose radius of 0.00635 m and a cone half-angle of 7 deg. The freestream conditions come from a test performed in the Passive Nosetip Technology [46] program designed to evaluate carbon-based nose tips for entry vehicles and are listed in Table 1. The cone axis is aligned with the freestream flow yielding an angle of attack equal to zero. The freestream unit Reynolds number and stagnation enthalpy are $Re_u = 7.3 \times 10^6/\text{m}$ and $h_{o,\infty} = 15.3$ MJ/kg, respectively. This is a high-enthalpy case, in which thermochemical nonequilibrium effects are significant and still present well downstream of the nose.

Each of the five mean-flow cases is listed in Table 2. Cases 1a and 1b have the same mean-flow profile, which is computed by the 11-species thermochemical nonequilibrium model with ablation boundary conditions. The surface-temperature profile computed from case 1 is used to set the wall temperature for cases 2–5. Case 2 is a five-species-air thermochemical nonequilibrium simulation with surface blowing. The five-species-air gas model is the exact same as the N_2, O_2, NO, N, and O components in the 11-species model. The imposed surface blowing has the same mass flux as case 1, but standard freestream air is blown instead of carbon products. Case 3 is the same as case 2, except there is no blowing at the surface. Also, the surface recombination of atomic oxygen [Eq. (8)] is retained for both cases 2 and 3. Cases 4 and 5 are both ideal-gas cases, which use the

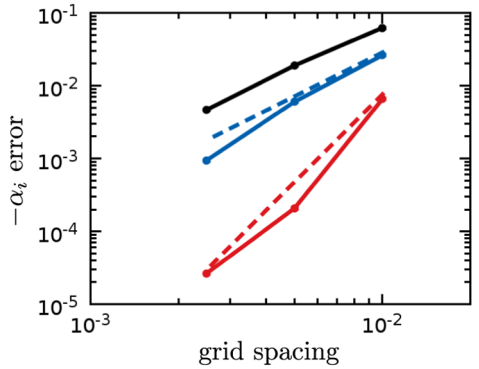

Fig. 3 Rate of convergence for schemes 1 (—), 2 (—), and 3 (—).

same nonequilibrium code with the source terms turned off, the vibration energy held constant, and the mass fractions held to their freestream values. This is done so the viscosity, thermal conductivity, etc., are calculated the exact same way for each of the five mean-flow cases. Case 4 has the same mass-flux profile as case 1 and case 2, whereas case 5 has no blowing.

Before moving further, the LST wall boundary conditions for each of these cases need to be covered briefly. The difference between cases 1a and 1b is the boundary condition used in the stability computations. In case 1a, the full linearized surface model for graphite pseudoablation is used, whereas in case 1b the linearized surface energy balance [Eq. (38)] is replaced with $\hat{T}_w = 0$. For cases 2–5, $\hat{T}_w = 0$ as the wall mean-flow temperature is set from case 1. For cases 2 and 3, the corresponding surface mass balances are linearized to provide conditions for species perturbations at the wall. Note that this is the same as described previously in Sec. IV.A, but the mass-flux terms, in which carbon species are produced, are dropped. For cases 4 and 5, the fluctuation of the composition is forced to zero (i.e., $c_s' = 0$).

Note that the same fourth-order LST code was used for each of the cases. For cases 2 and 3, only changes to the boundary conditions were required. For cases 4 and 5, all species and their perturbations, except N_2 and O_2, were forced to zero, the mean flow as well as the perturbation vibration temperature was forced to zero, the source terms and their derivatives were forced to zero, and k_V and D_s with their derivatives were forced to zero. Also, the boundary conditions for cases 4 and 5 were changed.

For each mean-flow case, the wall temperature is the same, that is, the wall temperature computed from case 1 is used to set all other cases. The wall temperature is shown in Fig. 4a. Note that there is a strong decrease in the wall temperature starting from the cone nose

Table 1 Freestream conditions

Parameter	Value
M_∞	15.99
ρ_∞	2.4093×10^{-2} kg/m^3
P_∞	2026.0 N/m^2
$c_{N_2,\infty}$	0.7635
$c_{O_2,\infty}$	0.2365

Table 2 Types of steady simulations

Case number	Type	Number of species	Blowing	LST boundary conditions
1a	Real gas	11	Ablation	Full linearized ablation
1b	Real gas	11	Ablation	$\hat{T}_w = 0$
2	Real gas	5	Yes	$\hat{T}_w = 0$
3	Real gas	5	No	$\hat{T}_w = 0$
4	Ideal gas	2	Yes	$\hat{T}_w = 0$
5	Ideal gas	2	No	$\hat{T}_w = 0$

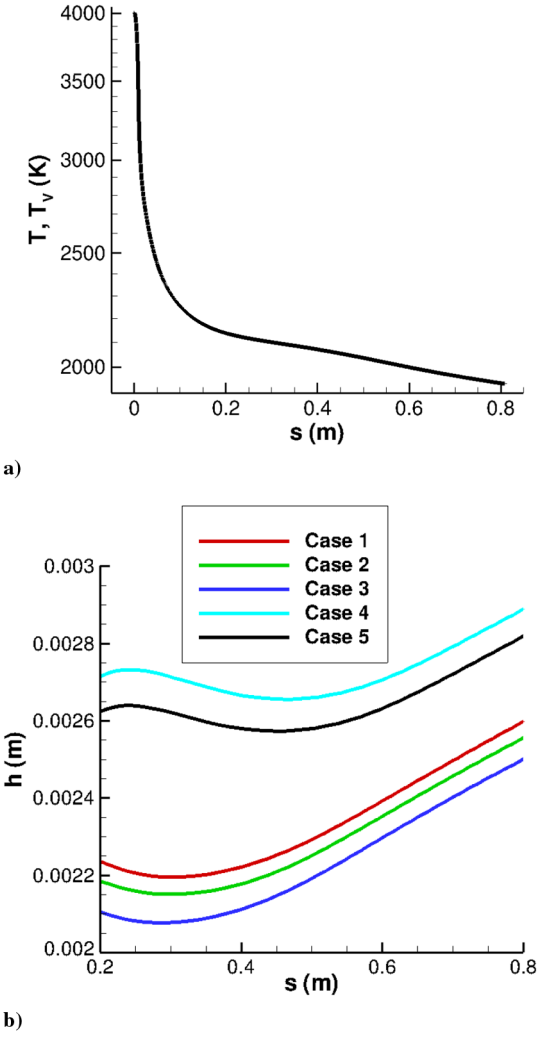

Fig. 4 Mean-flow a) wall temperature and b) total enthalpy boundary-layer thickness.

($s = 0$) and continuing downstream. This is common in zero angle-of-attack flows, as the highest wall temperature is commonly at the stagnation point, and then decreases downstream until the onset of turbulence. As the simulated mean flow is a laminar-flow simulation only, there is no onset of turbulence here, hence, no marked increase in wall temperature. Also note that, for $0.2 \geq s \geq 0.8$ m, $0.14 \geq T_w/T_0 \geq 0.13$, in which T_0 is the stagnation temperature.

Figure 4b shows the height of the boundary layer for a portion of the cone frustum. The height of the boundary layer was taken as the location where the total enthalpy was 99.5% of the total enthalpy immediately downstream of the bow shock in the wall-normal direction. Notice that, for a portion of the cone frustum, the boundary layer is decreasing in the downstream direction rather than increasing. At first, this may seem counterintuitive, as generally the boundary layer is continually increasing in the downstream direction. In this case, a favorable pressure gradient, combined with a strong decrease in wall temperature that cools the boundary layer and contracts the flow, decreases the height of the boundary layer. Along with the boundary layer, a supersonic blunted cone will produce an entropy layer. At the end of the domain ($s = 0.8$ m), the entropy layer has almost been fully swallowed by the boundary layer.

It has been shown in previous experimental research that the height of the boundary layer is nearly half the wavelength of the dominant second mode [47]. The phase velocity of the dominant second mode can be roughly approximated as the boundary-layer-edge velocity leading to $c_r \approx \text{const.} \approx \omega/\alpha_r \approx 2fh$. This shows that, as h decreases, f will increase to maintain a constant c_r. With this piece of information, it is expected that perhaps some lower frequencies will

become unstable for cases 1–3 before higher frequencies near $s = 0.2$ m due to the decrease in boundary-layer height.

Figure 5 shows the wall mass flux per area nondimensionalized by the freestream mass flux per area. As expected, the largest mass flux is at the stagnation point (approximately 1% of the freestream mass flux) corresponding to a maximum in wall temperature, in which the oxidation reactions as well as the sublimation reactions are all significant. Notice the surface mass flux drops nearly two orders of magnitude across the cone nose, and remains roughly the same order of magnitude along the cone frustum, indicating that outgassing effects would likely be most significant upstream in the nose region. This rapid drop of wall mass flux also corresponds to a rapid decrease in sublimation. The fact that there is still wall blowing in the cone frustum is due to the oxidation reactions. The wiggle near the nose of the cone is located directly downstream of the beginning of the cone frustum. The discontinuity in the surface curvature is likely the cause for the wiggle, and the appearance of the wiggle is exaggerated by the use of a logarithmic scale.

Before moving on to a linear-stability analysis, a comparison of all five mean-flow profiles is given for a single streamwise location ($s = 0.564$ m) in Fig. 6. In [18], the results of a grid-convergence study are given, showing that a proper grid is used for the mean flows. There is only a small difference in the streamwise-velocity profiles. The height of the velocity boundary layer is larger for cases 4 and 5, which is to be expected, as cases 4 and 5 are perfect gas. Similarly, the height of the temperature boundary layer is larger for the perfect-gas cases. Because cases 4 and 5 have a greater boundary-layer height, it is expected that their unstable frequency range will be lower than cases 1–3. It is also possible to compare the species densities between all five cases, noting that for perfect gas $\rho_{O_2} = c_{O_2,\infty}\rho$. At the wall, case 1 has less oxygen than the other cases. In case 1, ablation has introduced carbon products into the flow, and this far downstream most of the carbon is in the form of CO. This means that, for each carbon atom in CO, an oxygen atom is needed, which will reduce the density of oxygen and atomic oxygen for case 1 when compared to the other cases. This behavior is not seen in case 2 or 3, as there are no carbon-containing species. Near $y = 0.002$ m, cases 1, 2, and 3 begin to have the same density of oxygen, as CO has not diffused significantly beyond this wall-normal distance.

The mass concentration of CO and CO_2 for case 1 at multiple streamwise locations is shown in Fig. 7. They are shown because most of the mass from ablation is contained in CO, which is being

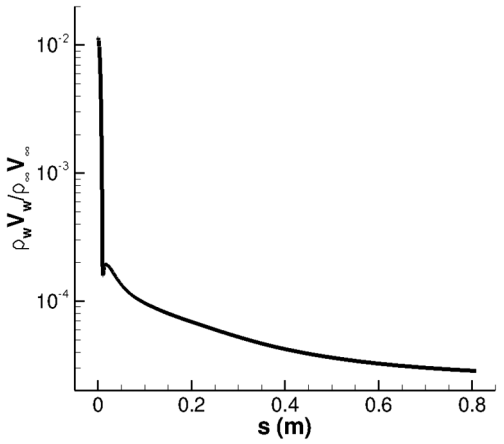

Fig. 5 Surface nondimensional mass flux.

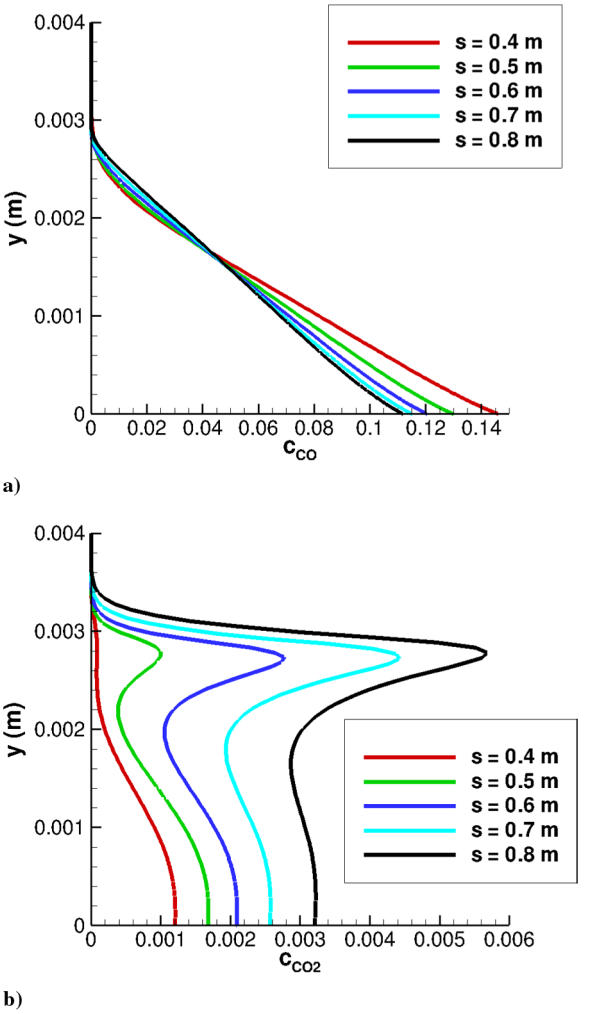

Fig. 7 Mass concentrations at multiple streamwise locations for case 1.

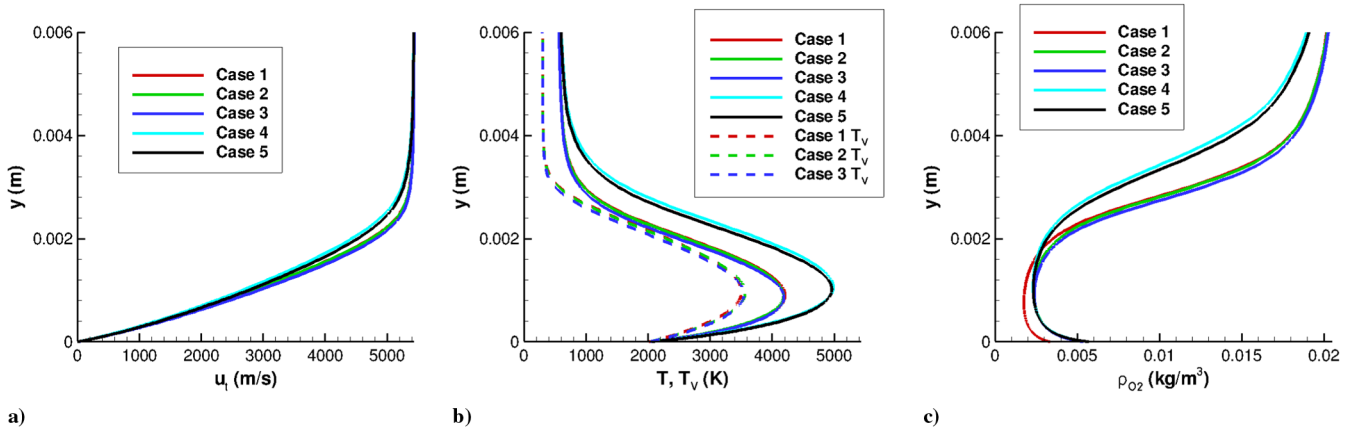

Fig. 6 Mean-flow-profile comparison at $s = 0.564$ m.

transferred to CO_2 as the flow moves downstream and cools. Likely, if carbon species are to have an effect on flow instability, it will be through CO and CO_2. Recall from Eqs. (6) and (7) that CO is created at the surface through surface reactions, and then can react with the freestream flow. However, CO_2 is formed solely through gas-phase reactions. The largest mass concentration for CO is found at the surface and decreases in the downstream direction. As the flow moves downstream, some CO_2 is recombining, which increases the mass concentration of CO_2 and decreases the mass concentration of CO. There is a peak in the mass fraction of CO_2 near $y = 0.003$ m, which is near the boundary-layer edge. This peak is due to lower temperatures near the boundary-layer edge.

B. Instability Characteristics of $M_\infty = 15.99$ Blunt Cone

LST gives information about what disturbance frequencies are unstable and the corresponding growth rates of those frequencies, but there is no information on the amplitude of the incoming disturbance. To estimate the boundary-layer transition using LST, the e^N transition criterion is used, which is defined as

$$e^N = \frac{A}{A_0} = \exp\left(-\int_{s_0}^{s} \alpha_i \, \mathrm{d}x\right) \tag{42}$$

Here, A is the integrated disturbance amplitude, A_0 is the initial amplitude, s_0 is the location where the disturbance first becomes unstable, and α_i is the spatial amplification rate. The integration is performed for a constant frequency ω. Note that a negative imaginary part of the wave number α results in disturbance growth, whereas a positive value results in disturbance decay. The N factor is specifically the exponent of e^N. In-flight transition N factors are commonly understood to be around 10. Malik [14] showed that 9.5 and 11.2 correlated with transition onset for two high-Mach-number flight tests. In ground test facilities, the transition N factor is usually lower.

After locating the second mode, it is possible to trace it upstream and downstream using LST to find the second-mode N factor. Figure 8 shows the N factor plots for each of the six cases. The case with the largest N factor is case 1a, in which the N factor is 5.97 at the exit of the domain. This means that, from the neutral point, the disturbance has grown 391 times. The corresponding frequency for this maximum N factor of case 1a is 500 kHz. The second largest N factor is found from case 1b, in which $N = 4.37$ and the corresponding frequency is 487.5 kHz. Recall that the only difference between cases 1a and 1b is the temperature-perturbation boundary condition, which is $\hat{T}_w = 0$ for case 1b. Comparing the N factors shows that the most amplified frequency for case 1a is nearly five times larger than the most amplified frequency for case 1b. Also, the frequency of the maximum second-mode N factor is shifted to a slightly lower frequency for case 1b. Hence, a change in only the temperature-perturbation boundary condition can have a significant effect on a hypersonic boundary layer's second mode.

From Figs. 8b and 8c, it is possible to note the differences that result due to changing the wall blowing from ablation to blowing air at the freestream mass concentration. Essentially, this would be measuring the effect of carbon species due to ablation in the boundary layer as opposed to only five-species air in the boundary layer. Recall from Fig. 6 that the difference in streamwise velocity and both temperatures for cases 1 and 2 is negligible, but there is some difference in the chemistry. For case 1b, the largest N factor is 4.37 at 487.5 kHz. For case 2, the maximum N factor is 4.46 at a frequency of 487.5 kHz. The difference between these two cases is small, with case 2 slightly more unstable than case 1. The frequency for the most amplified disturbance is the same for both cases. Therefore, for this test case, the carbon species in the boundary layer slightly damp the second-mode instability. These results are consistent with [48], in which it was found experimentally that a high-enthalpy CO_2 flow transitioned later than the corresponding N_2 or airflows at the same enthalpy.

To investigate these effects further, similar to [12], the sign of the heat of formation was changed for CO_2 and CO in the instability calculations for case 1b, whereas the mean flow remained the same. This effectively extracts heat from the flow, as compared to the nominal case, when CO_2 is produced, rather than adding heat. The results from this numerical experiment are shown in Fig. 9 for the frequency with the highest N factor in case 1b (487.5 kHz). Note that, by switching the sign for the heat of formation, an increased N factor, or growth rate, means the effects are stabilizing when the sign of the heat of formation is not switched. Also note that the only significant reaction including carbon species over the range shown is recombination of CO_2 denoted by $CO + O + M \rightarrow CO_2 + M$.

When only the sign of CO_2 is switched, the N factor is increased due to an increased growth rate. The increase in growth rate is slight and remains around 1–3% over the length of the unstable second-mode range. When the sign of the heat of formation is switched for both CO_2 and CO, the N factor is still higher when compared to the nominal case. However, CO has the opposite effect of CO_2. It is slightly decreasing the growth rate when compared to the case that only switches the sign of CO_2. To summarize these findings, switching the sign for the heat of formation of CO_2 measures the effect that production of CO_2, from CO and O, has on the flow. When the sign for the heat of formation of CO_2 is switched, it destabilizes the second mode. Therefore, when the sign is not switched, CO_2 stabilizes the second mode. This stabilizing effect is, however, quite slight for the given case, which likely explains the slight decrease in N factor from case 1b to case 2. It should be noted that it has been shown that the rate of $CO + O$ recombination is slow and atomic oxygen recombination can be much faster [49]. If this is the case, the flow may be composed of O_2 and CO, which can exist stably under these conditions. This could change the stabilizing effect shown here, which is likely due to the recombination of CO and O. Further simulations with different reactions and reaction rates would be needed to further elucidate this issue. However, for the reactions and reaction rates used here, it is likely that, as blowing increases, there will be more mass from carbon species in the boundary layer. Assuming that the same trend is followed, this will more strongly stabilize the boundary layer. Also, if the estimated ablation rates are low, it would be possible to predict transition in a second-mode-dominated graphite ablative flow by assuming the surface blowing to be composed of air rather than various carbon products.

It is also possible to isolate the effects of blowing on boundary-layer instability in a hypersonic real gas. Figures 8c and 8d show cases 2 and 3, in which case 2 has blowing and case 3 does not. The largest N factor for case 2 is 4.46 at 487.5 kHz. The largest N factor for case 3 is 4.12 at 500 kHz, which results in a decrease of the most amplified disturbance by 40%. Therefore, the boundary layer with blowing is destabilized compared to the boundary layer with no blowing. Note that the blowing profile is large upstream near the nose, but small downstream of the nose. So, it is conjectured that the strong blowing upstream has a larger effect than the near zero blowing downstream. Also, recall from Fig. 4b that the boundary-layer thickness is slightly less for case 3 as compared to case 4. It is likely that the slight shift in frequency between these two cases is due to the slight difference in the thickness of the boundary layer. The fact that the blowing is found to destabilize the second mode is consistent with previous research in [16] for a reacting boundary layer.

Similarly, blowing effects on a hypersonic boundary layer with an ideal-gas assumption can be seen by comparing Figs. 8e and 8f. The maximum N factor for case 4 is 1.88 at a frequency of 462.5 kHz, and the maximum N factor for case 5 is 1.81 at a frequency of 475 kHz. The difference between these two cases is minute, showing that, for the ideal-gas boundary layer, blowing has a negligible effect on boundary-layer stability in this particular case.

Finally, it is possible to isolate real-gas effects by comparing case 2 with case 4, and case 3 with case 5 (Figs. 8c and 8e, and Figs. 8d and 8f, respectively). The difference in maximum N factor between cases 2 and 4 is 2.58, which results in a disturbance that is 13 times larger for case 2. This is a significant difference. Here, the real gas causes the largest disturbance to grow an order of magnitude more than the ideal-gas case. Note also that the neutral points for unstable

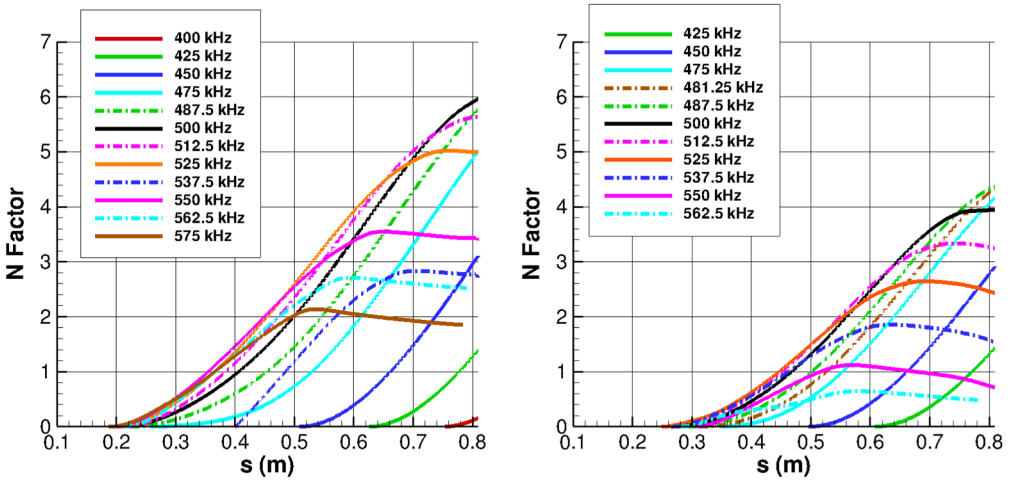

a) Case 1a

b) Case 1b

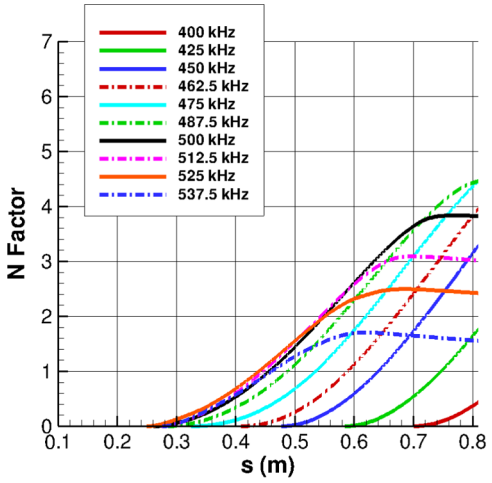

c) Case 2

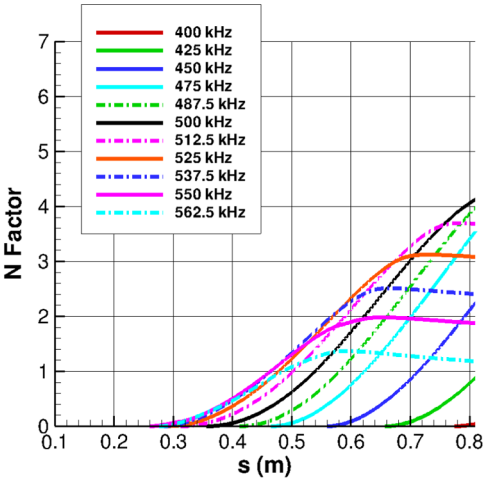

d) Case 3

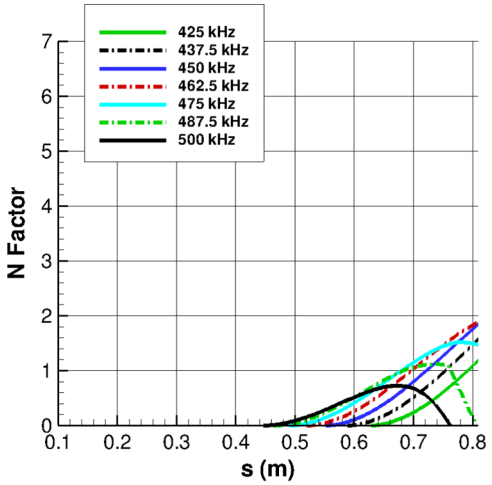

e) Case 4

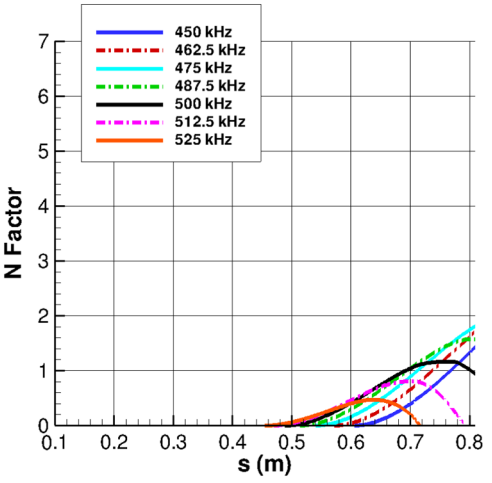

f) Case 5

Fig. 8 *N* factor comparison.

frequencies have moved downstream for the ideal-gas case when compared to the real-gas case. This is to be expected, as the height of the boundary layer is larger for the ideal-gas case (recall Fig. 4b). Similar results are seen by comparing cases 3 and 5. The difference in maximum N factor is 2.31, which gives a most amplified disturbance that is 10 times larger for case 3. Also, the start of the unstable frequency range for each frequency has again shifted downstream. Therefore, in this particular case, real-gas effects are destabilizing to the hypersonic boundary layer. Real-gas effects in both comparisons result in a maximum disturbance at the domain exit that is one order of magnitude larger than the corresponding ideal-gas case. Also, the neutral points shift downstream for the ideal-gas cases.

As seen in Eq. (42), the N factor is obtained by integrating the growth rate in the streamwise direction. By examining the growth rates corresponding with each N factor, it can be found how the growth rate is influencing the N factor. A growth-rate plot for each case is given in Fig. 10. Comparing cases 1a and 1b, the growth rate for each frequency is overall larger for case 1a. Also, the range along

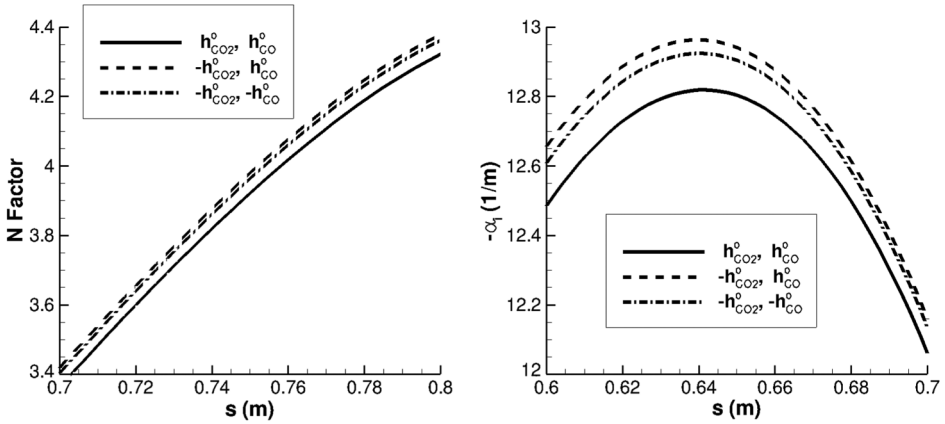

Fig. 9 *N* factor and growth-rate comparison of second mode varying h_{CO_2} and h_{CO}.

the cone for the unstable frequencies is larger for case 1a, that is, a frequency for case 1a is unstable over a larger length of the cone. Noting these differences, the difference in *N* factor between cases 1a and 1b is due to the larger growth rate and the larger range over which the frequencies are unstable.

Comparing cases 1b and 2, the growth rates for both cases, as well as the unstable ranges, are nearly the same. Looking specifically at the second mode at 487.5 kHz, the maximum growth rate is 12.82 at 0.64 m for case 1b, and is 12.98 at 0.63 m for case 2. This is a relative difference of 1.2% between these cases. This difference makes sense, as the maximum *N* factor of the two cases was nearly identical.

Comparing cases 2 and 3, it can be seen that the growth rate is nearly the same for both cases; therefore, the difference in *N* factor must be explained by a larger unstable range for case 2. Here, blowing is causing the unstable region to become larger for the most unstable frequencies in the domain.

The growth rates of cases 1a, 1b, 2, and 3 show that the highest frequency is not always the first unstable frequency. For example, notice Fig. 10c, in which the highest frequency included in the calculations is 537.5 kHz, and it crosses from stable to unstable at $s = 0.276$ m. Upstream of $s = 0.276$ m, there are lower frequencies than 537.5 kHz, such as 525 kHz, that are already unstable. This behavior is most likely due to the decreasing boundary-layer thickness causing some higher frequencies to become unstable later. This behavior is not seen for either case 4 or case 5, as there are no significant second-mode instabilities when the boundary layer is decreasing. Again, it is possible to analyze real-gas effects by comparing case 2 with case 4, and case 3 with case 5 (Figs. 10c and 10e, and Figs. 10d and 10f, respectively). Comparing cases 2 and 4, it can be seen that the growth rates for the real gas are larger than for the ideal gas. Also, the frequencies are unstable over a larger streamwise distance. Similarly, the growth rates for case 3 are much larger than for case 5, and the unstable range is larger for case 3. For this case, real-gas effects increase the disturbance growth rate, as well as increase the unstable range of the disturbance.

To analyze the effects of transverse curvature on the second mode only, the *N* factor was obtained using LST without the curvature terms for each case. Note that the mean flow is still computed with the transverse-curvature effect, and it is only in the instability waves in which transverse curvature is neglected. Figure 11 shows the *N* factor comparison of the second mode at a frequnecy of 487.5 kHz for case 1b with and without curvature. The largest *N* factor computed with the transverse-curvature terms neglected is 4.68 for the 487.5 kHz second mode. This results in a 37% amplification compared to case 1b, in which the transverse-curvature terms are included. The frequency for the largest *N* factor is not changed. This trend is the same for each of the cases. For each case, excluding the transverse-curvature terms results in a larger *N* factor, that is, the second mode is destabilized, but the frequency remains the same. These results are consistent with previous instability calculations using a perfect gas [40] and a chemically reacting flow [8].

VII. Linear-Stability Analysis of the Reentry-F $M_\infty = 19.925$ Blunt Cone

This blunt-cone case corresponds to a flight test, called Reentry-F, designed to study the effects of a turbulent boundary layer on surface heating. High-quality transition data are available from this experiment at multiple trajectory points. The vehicle geometry is a 5 deg cone with a nominal nose radius of 2.54 mm [3]. The freestream conditions simulated here are for the vehicle at 100 kft and are given in Table 3. The blunt-cone nose was composed of ATJ graphite from the nose tip to 0.22 m downstream along the cone axis. During the flight, the nose cone ablated and changed shape; thus, an estimate for the ablated nose-tip radius at the given flight altitude is needed. The same estimated nose-tip radius (3.1×10^{-3} m) from [14] is used here. The remaining straight-cone portion was composed of beryllium. Surface-temperature measurements are available along the beryllium portion of the cone [50]. These conditions have been studied extensively by previous researchers [14,15], in which the most unstable frequencies and their *N* factors at transition onset were calculated for multiple gas models. However, their analysis neglected outgassing due to an ablating nose cone and carbon species in the freestream due to ablation, which are accounted for in the current work.

A. Steady-State Solutions of Reentry-F $M_\infty = 19.925$ Blunt Cone

Two separate mean-flow simulations were run. The first case, called case 6, is a five-species thermochemical nonequilibrium simulation. This simulation is similar to the mean-flow simulations run in [14,15]. The surface temperature is set from experimental results downstream of the ablating nose, and an estimate from [14] is used for the nose temperature. Noncatalytic conditions at the surface are used for each species across the entire length of the vehicle. The second case, called case 7, is an 11-species thermochemical nonequilibrium simulation. This simulation accounts for the ablating nose through inclusion of the surface-chemistry model described in Sec. III. Downstream of the ablating nose, the experimental wall temperature is used and a noncatalytic condition is enforced at the surface.

Figure 12 shows a comparison of the streamwise velocity between case 6 and case 7 [14,15]. Different computational grids were used for the different cases, making the comparison at slightly different streamwise locations. However, the comparison between the cases is quite good. There are only slight differences between each of the cases. There is a difference between case 6 and case 7, but it is not visible in the plot. This shows that the inclusion of the ablating nose cone has only a slight effect on the mean-flow profile of wall-tangent velocity at the domain outlet.

The wall temperature for cases 6 and 7 is shown in Fig. 13a. The wall temperature used in [14,15] is the same as case 6. The maximum wall temperature at the stagnation point for both cases is nearly the same. The wall temperature for case 7 drops quicker than case 6 near

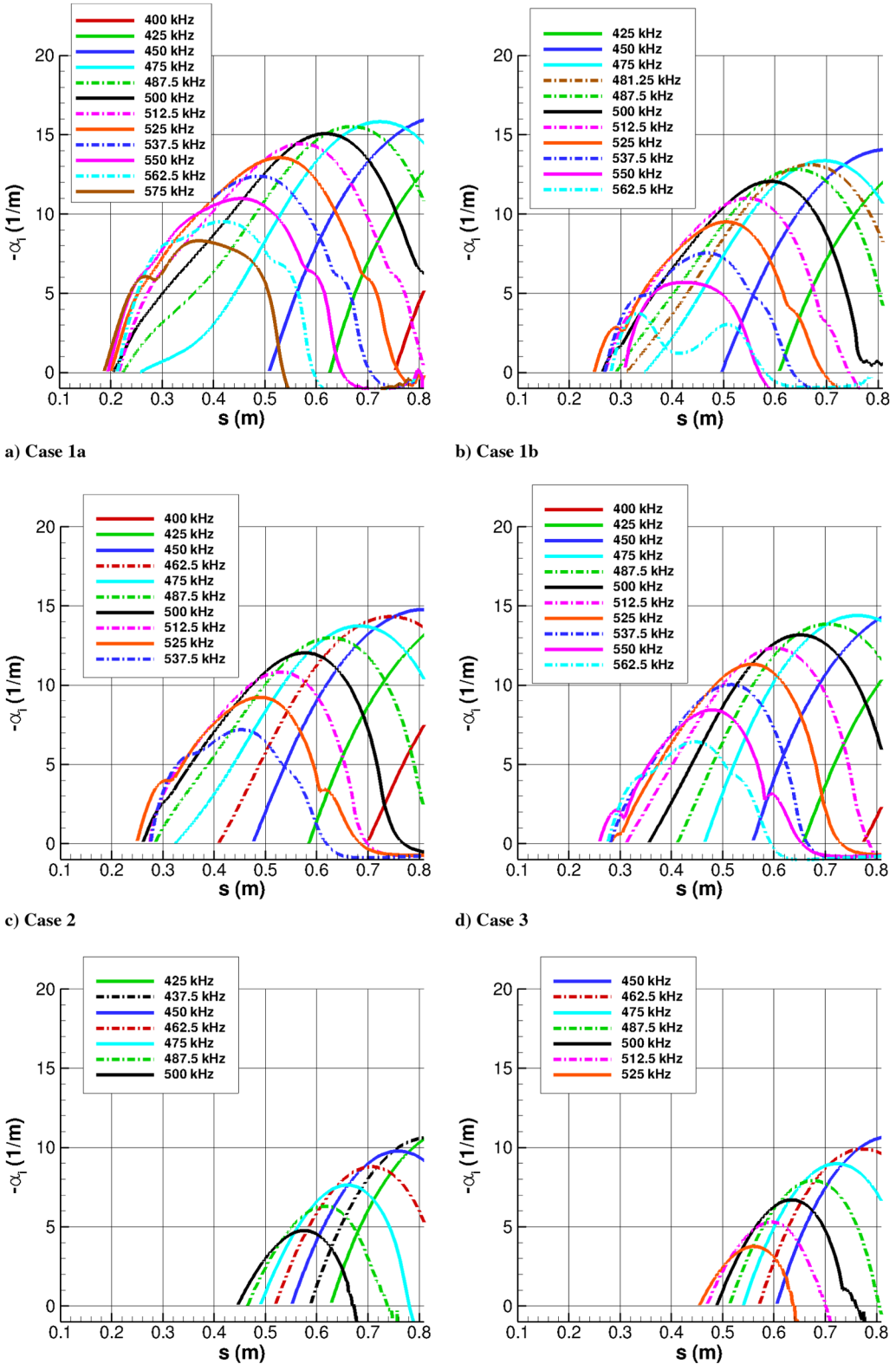

Fig. 10 Growth-rate ($-\alpha_i$) comparison.

the stagnation point, and then almost levels off near $s = 0.22$ m, which corresponds to the end of the ablating nose cone. After the ablating nose cone, case 7 is fit to the experimentally measured wall temperature and is the same as case 6 downstream of $s = 1.0$ m. The main difference between these two cases is the brief leveling off of the wall temperature before dropping again in case 7, which is not seen in case 6. Figure 13b shows the comparison of the computed wall heat flux between case 6 and case 7 [14,15]. This comparison also has corresponding experimental data. For [14,15], there is a noticeable rise in heat flux downstream of the nose near $s = 0.1$ m that is only slightly present in case 6 and not present at all in case 7. It is likely that this rise in heat flux is due to the estimated wall-temperature distribution and likely exacerbated by a lack of streamwise grid in this area of rapid wall-temperature decrease. The heat flux for case 7 is more natural. It is a maximum at the stagnation point and decreases downstream. There is a jump near $s = 0.22$ m due to the

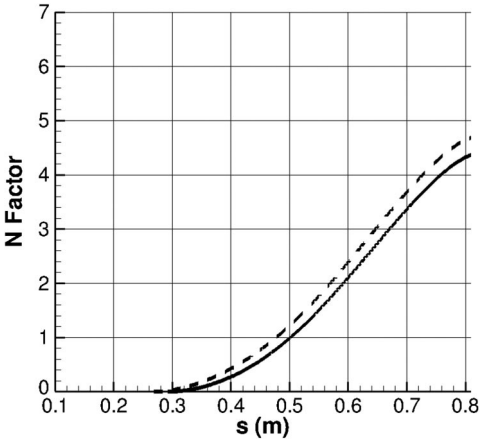

Fig. 11 ***N*** **factor comparison for case 1b with and without transverse curva- ture.**

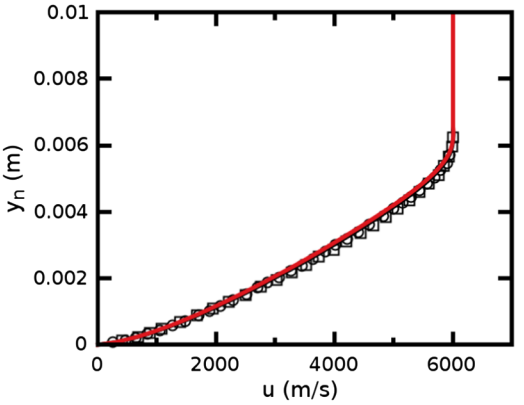

Fig. 12 Comparison of streamwise velocity; case 6 at $s = 3.21$ m denoted by —, case 7 at $s = 3.21$ m denoted by —, [14] at $s = 3.24$ m denoted by □, and [15] at $s = 3.26$ denoted by ○.

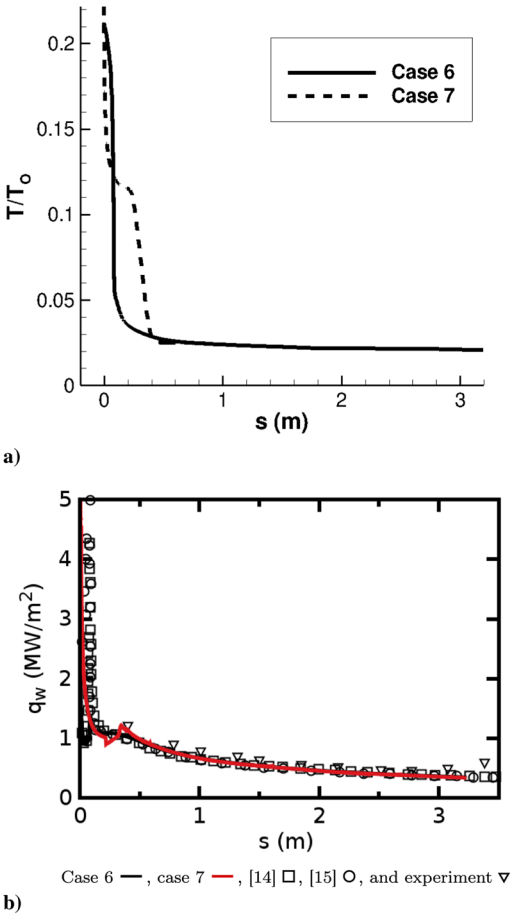

Fig. 13 Comparison of a) wall temperature and b) heat flux.

discontinuity in surface boundary conditions. After this discontinuity, the heat flux increases slightly due to recombination of species, especially CO_2, near the wall. This increase in heat flux more accurately matches the experimentally measured heat flux than the other cases. Downstream of $s = 1.0$ m, each of the cases heat fluxes lie on top of each other.

The translation–rotation temperature and the vibration temperature at several streamwise locations are shown in Fig. 14. Each profile has the same wall temperature except the station at $x = 0.22$ m, which is at the end of the nose cone. At this station, both temperatures are higher for case 7. Moving downstream starting from $x = 1.76$ m, the translation–rotation temperature shows little variation between cases 6 and 7. Each of the profiles for case 7 is shifted away from the wall due to a thickening of the boundary layer from blowing, but the shift is small. For the vibration temperature, there is a larger difference. For case 6, the vibration temperature is consistently less, which is most likely due to the existence of CO_2, as well as a thicker boundary layer, for case 7. From these mean-flow results, it is likely that temperature effects on flow instability will be more pronounced upstream near the nose cone where the difference between the cases is the largest.

The surface mass flux nondimensionalized by the freestream mass flux is given in Fig. 15. The mass flux is a maximum at the stagnation point where it is 2% of the freestream mass flux. The most significant blowing occurs on the hemispherical nose tip. Downstream of the hemispherical nose tip on the straight portion of the cone, the mass flux is less than 0.1% of the freestream mass flux. It seems likely that any effects on flow instability due to blowing would stem from the higher mass flux on the nose tip rather than the lower mass flux on the straight portion of the nose cone.

The mass fractions of CO and CO_2 for case 7 are shown in Fig. 16. Of the gas species containing carbon, only CO and CO_2 are shown because they are the most massive. Each station is normal to the surface at a given location. The first location corresponds to the end of the ablating nose cone. At this station, carbon in the freestream is mainly in the form of CO, and it makes up approximately 10% of the fluid mass near the surface. At $x = 0.50$ m, CO accounts for roughly 1% of the mass near the center of the boundary layer. Downstream of $x = 1.00$ m, the mass of CO has become less than 0.1% and continues to decrease downstream. On the other hand, CO_2 is less than 0.1% at the exit of the nose cone due to the high surface temperature, but increases rapidly to 5% of the mass at the wall at $x = 0.5$ m, and then decreases gradually downstream. Downstream of $x = 0.50$ m, there is not a significant amount of carbon in any species except CO_2. Therefore, it is expected that CO_2 will impact flow instability more than CO near the experimentally measured transition location.

Table 3 Freestream conditions for Reentry-F

Parameter	Value
M_∞	19.925
ρ_∞, kg/m^3	0.01672
p_∞, N/m^2	1099.0
c_{N_2}	0.767
c_{O_2}	0.233

B. Instability Characteristics of Reentry-F $M_\infty = 19.925$ Blunt Cone

N factor plots for both cases 6 and 7 are shown in Fig. 17. The location of transition onset, as indicated by the rise in the experimental heat flux, is $s = 2.9$ m. This location is marked on the figures. The largest *N* factor at this streamwise location for case 6 is 7.8 at a frequency of 260 kHz. Compare this with the value of 8.1 at a

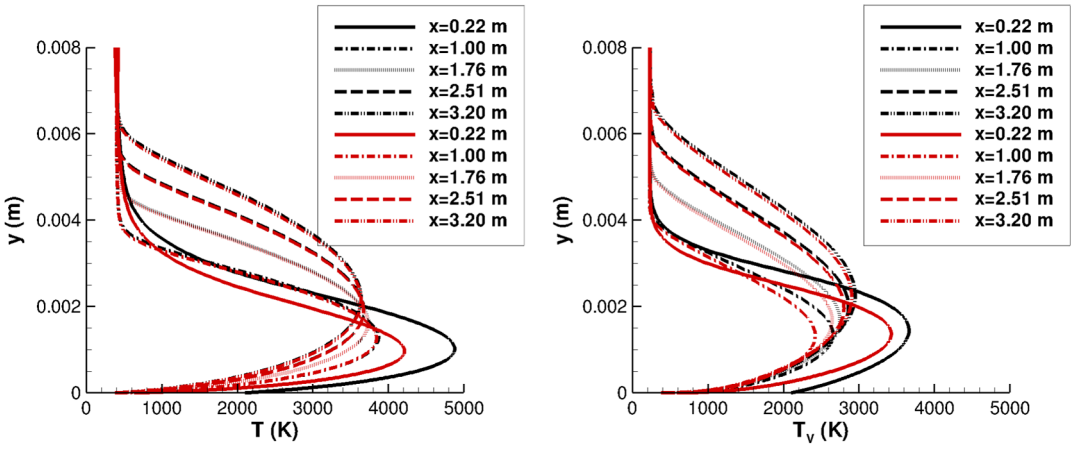

Fig. 14 Wall-normal profiles for cases 6 (—) and 7 (—).

frequency of 240 kHz obtained in [14] using LST and a finite rate chemistry model. Considering the differences in the model, the N factor at transition is quite close. In [15], an N factor of 8.7 at a frequency of 250 kHz was obtained using a similar thermochemical nonequilibrium model, but the PSEs were used rather than LST to compute the flow instability. With a similar gas model, one would expect the comparison of the N factor to be closer; however, N factors computed from PSE are generally larger than those computed using LST, and so the difference is not unusual. Overall, the stability calculations agree reasonably well with previous stability calculations for the same geometry and flow conditions.

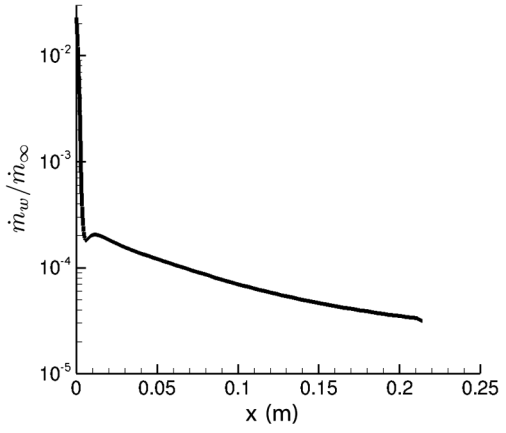

Fig. 15 Surface mass flux for case 7.

The largest N factor at $s = 2.9$ m for case 7 is 7.7 at a frequency of 250 kHz. This is not a large difference from the N factor of 7.8 obtained in case 6, and may be near to the numerical noise of the simulation. However, this slight damping effect is consistent along the cone downstream of $s = 1.0$ m, making it unlikely to be significantly affected by numerical noise. Also, the frequency that leads to transition for case 7 is 10 kHz lower than case 6. This same stabilizing behavior was seen in Sec. VI.B, in which the carbon chemistry obtained from ablation was shown to slightly stabilize the flow as compared to a simulation with only five-species air.

Upstream of $s = 1.0$ m, the ablating nose cone has increased the N factor. The largest difference is 68% at $s = 0.8$ m. Here, the blowing effects are stronger than at $s = 2.9$ m, as the location is closer to the nose cone. Recall from Fig. 10 that blowing effects over a $M_\infty = 16$ blunt cone were shown to destabilize the second mode. It is likely that this close to the nose cone, the blowing effects are destabilizing the second mode more than the carbon species are stabilizing the second mode. This results in a net increase in the most amplified second mode upstream of $s = 1.0$ m.

Figure 18 shows a comparison of the growth rate and phase velocity between case 6 and case 7 for two frequencies. For the 460 kHz instability of case 6, there is clear second-mode instability denoted by a large positive growth rate and a change in the sign of the phase-velocity slope near $s = 0.5$ m. This change in phase-velocity slope occurs near the synchronization location of the fast and slow acoustic modes. There is also a clearly defined third-mode unstable region denoted by a large positive growth rate and a change in the sign of the phase-velocity slope near $s = 3.0$ m. This region of second-mode growth, and then a later region of third-mode growth, was also seen in [14,15].

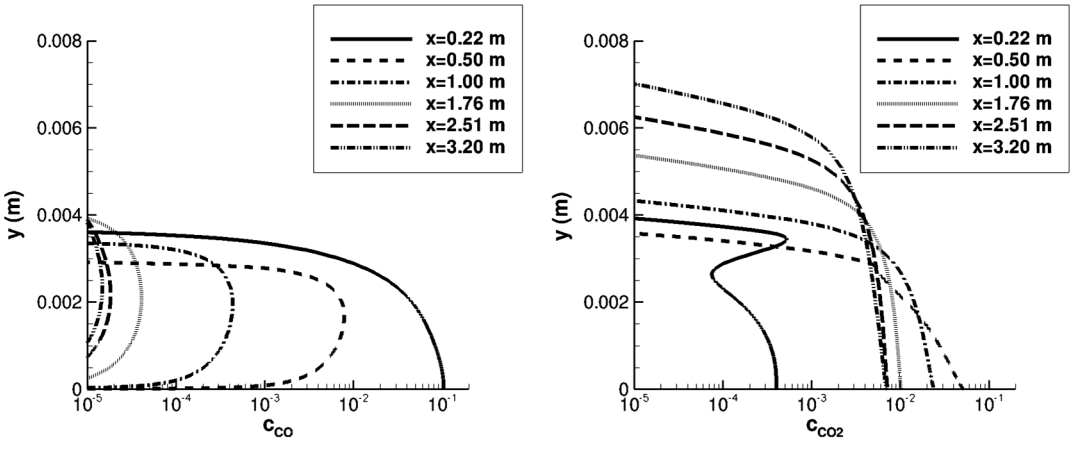

Fig. 16 Wall-normal profiles for case 7 of a) c_{CO} and b) c_{CO_2}.

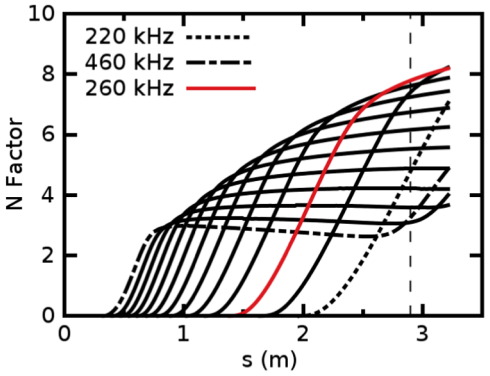

a) Case 6

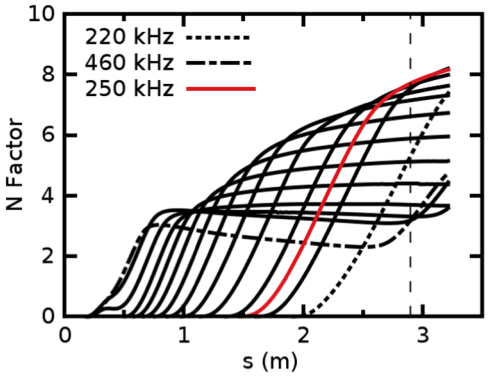

b) Case 7

Fig. 17 *N* factor comparison.

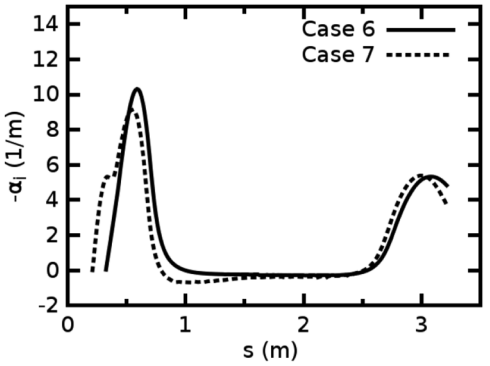

a)

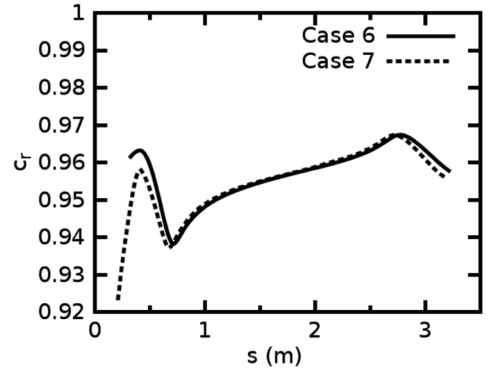

b)

Fig. 18 Comparison of LST at 460 kHz between cases 6 and 7.

Comparing the second-mode-growth region for cases 6 and 7, the maximum second-mode growth rate for case 7 is less than case 6. However, the maximum second-mode growth rate and location of initial instability growth have shifted upstream for case 7. This creates a larger region over which the second mode is unstable. Even though the maximum amplification has decreased, the increased extent over which the second mode is unstable results in a higher N factor for case 7. Also, there is a jog in the growth rate for case 7 near $s = 0.5$ m, which is likely due to the rapid change in temperature slope at the same streamwise location and not to a switch from first to second modes. The third mode is affected by a shift upstream while the maximum growth rate is unaffected.

The comparison of growth rate and phase velocity for the 260 kHz instability between cases 6 and 7 has only slight differences. Only the second-mode instability is present for this frequency over the portion of the cone simulated. The unstable region begins near $s = 1.5$ m, and is shifted slightly upstream for case 7. There is very little variation in shape between the cases for both growth rate and phase velocity. Essentially, both cases give the same result with case 7 shifted slightly upstream of case 6. This is likely due to the slight increase in boundary-layer thickness of case 7 due to the outgassing in the nose cone. This is why case 7 has a lower frequency for the largest N factor at $s = 2.9$ m.

It has been shown that including the ablative nose cone affects frequencies differently. For higher frequencies, whose second-mode unstable regions are near the nose cone, such as the 460 kHz frequency, the location of initial instability growth is moved upstream, and there is a slight damping of the second mode. The growth rate of the third mode is unaffected with a slight upstream shift. For lower frequencies, whose second-mode unstable region is far downstream of the ablating nose cone, such as the 260 kHz frequency, the growth rate and phase velocity of the instability are the same except for a slight upstream shift. It is likely that this upstream shift is attributable to the increase in boundary-layer thickness caused by the ablating nose cone.

These findings indicate that including the effects of the ablating nose cone is stabilizing to the second-mode instability when the second mode is far downstream of the nose. Near the nose cone, blowing effects cause an increase in the region of instability and a decrease in the maximum amplification rate, which do result in a higher N factor. However, assuming that the transition location is far enough downstream of the ablating nose cone, the effects of the ablating nose cone are to slightly stabilize the second mode. It should be noted that an LST analysis, like the one performed here, does not include the receptivity process, which is likely different when the ablating nose cone is included. This would result in different initial amplitudes to the eigenmode-growth process for cases 6 and 7. However, N factor correlation, which is derived from an eigenmode analysis without including receptivity, has been shown to reliably correlate with transition onset. This correlation implies that transition is strongly affected by eigenmode growth, and the effect that the ablating nose cone has on eigenmode growth, for the conditions tested, is small. Therefore, this small difference in N factors and frequencies that lead to transition seems to indicate that, for these flight conditions, the nose-cone effects can be safely neglected to obtain a reasonable estimate of the value of the N factor and the corresponding frequency at the transition location.

VIII. Conclusions

The effects of surface-ablation-induced outgassing in the absence of surface recession and roughness on the instability of a real- and ideal-gas hypersonic boundary layer have been studied using LST. Before studying the instability physics, a new thermochemical nonequilibrium linear-stability-theory code with carbon species due to graphite ablation and a linearized surface model for graphite pseudoablation was developed and validated. The derivation of the linear-stability-theory coefficient matrices follows the work of Hudson [11]. An 11-species gas model was used, in which five-species model air and six more species are used to model the graphite-ablation effects. The derivative operators were discretized using Lagrange polynomials in physical space, in which, for a five-point stencil, the order of error was shown to be four. A linearized surface model for graphite pseudoablation applicable to parallel and nonparallel flows is given. The code was then validated with results

from a DNS of flowfield disturbances over a blunt cone. The comparison of the eigenfunction amplitudes was good. As DNS and LST are two dramatically different methods to analyze linear instabilities in a boundary layer, the good agreement obtained between the methods shows that they have been implemented correctly.

To study hypersonic boundary-layer instability physics, multiple simulations were run for two separate geometries and freestream conditions. Five simulations were run for a 7 deg half-angle blunt cone at Mach 15.99, and two simulations were run for a 5 deg half-angle blunt cone at Mach 19.925. The mean flows, when applicable, had the same blowing and wall-temperature profiles so that the effects of a real gas, blowing, and carbon species on hypersonic boundary-layer instability could be isolated and analyzed. N factors for different unstable frequencies and their corresponding growth rates were computed. For the first set of conditions, it was shown that changing the temperature-perturbation boundary condition for an ablative flow has a strong effect on boundary-layer instability. For these freestream conditions, the real-gas effects are strongly destabilizing. The amplification rates are higher and the instability zones are longer for a real gas. The effects of carbon species on second-mode instability are slightly stabilizing when compared to a similar case with only five-species air. Blowing was seen to be slightly destabilizing for a real gas, but its effect was negligible on an ideal gas. As a consequence to these results, a real gas should be considered in transition prediction for vehicles with ablative surfaces. If a real gas is not considered, the estimated transition location may be severely overpredicted.

For the second set of conditions, the inclusion of the ablating nose cone was shown to increase the region of second-mode growth near the nose cone. Away from the nose cone, the second mode was relatively unaffected. It was shown that the exclusion of the nose-cone effects gives a reasonable estimate of the frequency that leads to transition and its N factor at transition for the given case.

Acknowledgments

The research was supported in part by the U.S. Air Force Office of Scientific Research (AFOSR)/NASA National Center for Hypersonic Research in Laminar–Turbulent Transition and also the U.S. Department of Defense (DoD) through the National Defense Science and Engineering Graduate Fellowship Program. The computations were run partly on XSEDE resources provided by the Texas Advanced Computing Center under grant number TG-ASC100002 supported in part by the National Science Foundation. Also, this work was supported in part by a grant of computer time from the DoD High Performance Computing Modernization Program at the U.S. Air Force Research Laboratory, DoD Supercomputing Resource Center. The views and conclusions contained herein are those of the authors and should not be interpreted as necessarily representing the official policies or endorsements either expressed or implied, of the AFOSR or the U.S. Government.

References

[1] Ungar, E., "Ablation Thermal Protection Systems," *Science*, Vol. 54, No. 1, 1967, pp. 740–744. doi:10.1126/science.158.3802.740

[2] Carter, H., Raper, J., Hinson, W., and Morris, W., "Basic Measurements from a Turbulent-Heating Flight Experiment on a 5° Half-Angle Cone at Mach 20 (Reentry F)," NASA TM-X-2308, 1971.

[3] Johnson, C., Stainback, P., Wicker, K., and Bony, L., "Boundary-Layer Edge Conditions and Transition Reynolds Number Data for a Flight Test at Mach 20 (Reentry F)," NASA TM X-2584, 1972.

[4] Sherman, M., and Nakamura, T., "Flight Test Measurements of Boundary-Layer Transition on a Nonablating 22-Degree Cone," *Journal of Spacecraft and Rockets*, Vol. 7, No. 2, 1970, pp. 216–219. doi:10.2514/3.29907

[5] Schneider, S., "Effects of Roughness on Hypersonic Boundary-Layer Transition," *Journal of Spacecraft and Rockets*, Vol. 45, No. 2, 2008, pp. 193–209. doi:10.2514/1.29713

[6] Mack, L., "Boundary Layer Linear Stability Theory," AGARD Rept. 709, 1984.

[7] Malik, M., "Numerical Methods for Hypersonic Boundary Layer Stability," *Journal of Computational Physics*, Vol. 86, No. 2, 1990, pp. 376–413. doi:10.1016/0021-9991(90)90106-B

[8] Chang, C., Vinh, H., and Malik, M., "Hypersonic Boundary-Layer Stability with Chemical Reactions Using PSE," AIAA Paper 1997-2012, June 1997.

[9] Stuckert, G., and Reed, H., "Linear Disturbances in Hypersonic, Chemically Reacting Shock Layers," *AIAA Journal*, Vol. 32, No. 7, 1994, pp. 1384–1393. doi:10.2514/3.12206

[10] Hudson, M., Chokani, N., and Candler, G., "Linear Stability of Hypersonic Flow in Thermochemical Nonequilibrium," *AIAA Journal*, Vol. 35, No. 6, 1997, pp. 958–964. doi:10.2514/2.204

[11] Hudson, M., "Linear Stability Theory of Hypersonic, Chemically Reacting Viscous Flow," Ph.D. Thesis, North Carolina State Univ., Raleigh, NC, 1996.

[12] Johnson, H., Seipp, T., and Candler, G., "Numerical Study of Hypersonic Reacting Boundary Layer Transition on Cones," *Physics of Fluids*, Vol. 10, No. 10, 1998, pp. 2676–2685. doi:10.1063/1.869781

[13] Ma, Y., and Zhong, X., "Receptivity to Freestream Disturbances of a Mach 10 Nonequilibrium Reacting Oxygen Flow over a Flat Plate," AIAA Paper 2004-0256, Jan. 2004.

[14] Malik, M., "Hypersonic Flight Transition Data Analysis Using Parabolized Stability Equations with Chemistry Effects," *Journal of Spacecraft and Rockets*, Vol. 40, No. 3, 2003, pp. 332–344. doi:10.2514/2.3968

[15] Johnson, H., and Candler, G., "Hypersonic Boundary Layer Stability Analysis Using PSE-Chem," AIAA Paper 2005-5023, June 2005.

[16] Johnson, H., Gronvall, J., and Candler, G., "Reacting Hypersonic Boundary Layer Stability with Blowing and Suction," AIAA Paper 2009-938, Jan. 2009.

[17] Li, F., Choudhari, M., Chang, C., and White, J., "Boundary Layer Transition over Blunt Hypersonic Vehicles Including Effects of Ablation-Induced Out-Gassing," AIAA Paper 2011-3303, June 2011.

[18] Mortensen, C., and Zhong, X., "Simulation of Second-Mode Instability in a Real-Gas Hypersonic Flow with Graphite Ablation," *AIAA Journal*, Vol. 52, No. 8, 2014, pp. 1632–1652. doi:10.2514/1.J052659

[19] Chen, Y., and Milos, F., "Navier–Stokes Solutions with Finite Rate Ablation for Planetary Mission Earth Reentries," *Journal of Spacecraft and Rockets*, Vol. 42, No. 6, 2005, pp. 961–970. doi:10.2514/1.12248

[20] Wang, X., and Zhong, X., "A High-Order Shock-Fitting Non-Equilibrium Flow Solver for DNS of Strong Shock and Turbulence Interactions," *Seventh International Conference on Computational Fluid Dynamics*, ICCFD7 Paper 2307, July 2012.

[21] Prakash, A., Parsons, N., Wang, X., and Zhong, X., "High-Order Shock-Fitting Methods for Direct Numerical Simulation of Hypersonic Flow with Chemical and Thermal Nonequilibrium," *Journal of Computational Physics*, Vol. 230, No. 23, 2011, pp. 8474–8507. doi:10.1016/j.jcp.2011.08.001

[22] Park, C., *Nonequilibrium Hypersonic Aerothermodynamics*, Wiley, New York, 1990, pp. 24, 57–60, 326.

[23] Dolton, T., Maurer, R., and Goldstein, H., "Thermodynamic Performance of Carbon in Hyperthermal Environments," AIAA Paper 1968-754, June 1968.

[24] McBride, B., Heimel, S., Ehlers, J., and Gordon, S., "Thermodynamic Properties to 6000° for 210 Substances Involving the First 18 Elements," NASA SP-3001, 1963.

[25] Park, C., "On Convergence of Computation of Chemically Reacting Flows," AIAA Paper 1985-0247, Jan. 1985.

[26] Bhutta, B., and Lewis, C., "Low-to-High Altitude Predictions of Three-Dimensional Ablative Reentry Flowfields," AIAA Paper 1992-0366, Jan. 1992.

[27] Park, C., Howe, J., Jaffe, R., and Candler, G., "Chemical-Kinetic Problems of Future NASA Missions," AIAA Paper 1991-0464, Jan. 1991.

[28] Lee, J., "Basic Governing Equations for the Flight Regimes of Aeroassisted Orbital Transfer Vehicles," *Thermal Design of Aeroassisted Orbital Transfer Vehicles*, Vol. 96, edited by Nelson, H. F., AIAA, New York, 1985, pp. 3–53.

[29] Blottner, F., Johnson, M., and Ellis, M., "Chemically Reacting Gas Viscous Flow Program for Multi-Component Gas Mixtures," Sandia National Lab. SC-RR-70-754, Albuquerque, NM, 1971.

[30] Gupta, R., Lee, K., and Sutton, K., "Viscous-Shock-Layer Solutions with Coupled Radiation and Ablation Injection for Earth Entry," AIAA Paper 1990-1697, June 1990.

[31] Candler, G., "Computation of Thermo-Chemical Nonequilibrium Martian Atmospheric Entry Flow," AIAA Paper 1990-1695, June 1990.
[32] Wilke, C., "A Viscosity Equation for Gas Mixtures," *Journal of Chemical Physics*, Vol. 18, No. 4, 1950, pp. 517–519. doi:10.1063/1.1747673
[33] Suzuki, T., Fujita, K., Ando, K., and Sakai, T., "Experimental Study of Graphite Ablation in Nitrogen Flow," *Journal of Thermophysics and Heat Transfer*, Vol. 22, No. 3, 2008, pp. 382–389. doi:10.2514/1.35082
[34] Park, C., and Bogdanoff, D., "Shock-Tube Measurements of Nitridation Coefficient of Solid Carbon," *Journal of Thermophysics and Heat Transfer*, Vol. 20, No. 3, 2006, pp. 487–492. doi:10.2514/1.15743
[35] Anna, A., Alkandry, H., and Boyd, I., "Computational Modeling of Gas–Surface Interactions for High-Enthalpy Reacting Flows," AIAA Paper 2013-0187, Jan. 2013.
[36] Driver, D., and MacLean, M., "Improved Predictions of PICA Recession in Arc Jet Shear Tests," AIAA Paper 2011-141, Jan. 2011.
[37] Park, C., "Effects of Atomic Oxygen on Graphite Ablation," *AIAA Journal*, Vol. 14, No. 11, 1976, pp. 1640–1642. doi:10.2514/3.7267
[38] Baker, R., "Graphite Sublimation Chemistry Nonequilibrium Effects," *AIAA Journal*, Vol. 15, No. 10, 1977, pp. 1391–1397. doi:10.2514/3.60806
[39] Palmer, H., and Mordecai, S., *Chemistry and Physics of Carbon*, Marcel Dekker, New York, 1968, p. 126.
[40] Malik, M., and Spall, R., "On the Stability of Compressible Flow Past Axisymmetric Bodies," *Journal of Fluid Mechanics*, Vol. 228, July 1991, pp. 443–463. doi:10.1017/S002211209100277X
[41] Klentzman, J., Ulker, E., and Tumin, A., "Projection of the Solution of the Linearized Navier–Stokes Equations in Reacting High Speed Boundary Layers onto Discrete Modes," AIAA Paper 2012-3149, June 2012.
[42] Chang, C.-L., "Langley Stability and Transition Analysis Code (LASTRAC) Version 1.2 User Manual," NASA TM-2004-213233, 2004.
[43] Anderson, E., Bai, Z., Bischof, C., Blackford, S., Demmel, J., Dongarra, J., Du Croz, J., Greenbaum, A., Hammarling, S., McKenney, A., and Sorensen, D., *LAPACK Users' Guide*, 3rd ed., Soc. for Industrial and Applied Mathematics, Philadelphia, 1999, pp. 9–53.
[44] Stuckert, G., "*Linear Stability Theory of Hypersonic, Chemically Reacting Viscous Flow*," Ph.D. Thesis, Arizona State Univ., Tempe, AZ, 1991.
[45] Mortensen, C., and Zhong, X., "Numerical Simulation of Graphite Ablation Induced Outgassing Effects on Hypersonic Boundary Layer Receptivity over a Cone Frustum," AIAA Paper 2013-0522, Jan. 2013.
[46] Wool, M., "Final Summary Report: Passive Nosetip Technology (PANT) Program," SAMSO/RSSE SAMSO TR-75-250, 1975.
[47] Stetson, K., Thompson, E., Donaldson, J., and Siler, L., "Laminar Boundary Layer Stability Experiments on a Cone at Mach 8, Part 2: Blunt Cone," AIAA Paper 1984-0006, Jan. 1984.
[48] Adam, P., and Hornung, H., "Enthalpy Effects on Hypervelocity Boundary-Layer Transition: Ground Test and Flight Data," *Journal of Spacecraft and Rockets*, Vol. 34, No. 5, 1997, pp. 614–619. doi:10.2514/2.3278
[49] Sepka, S., Chen, Y.-K., Marschall, J., and Copeland, R., "Experimental Investigation of Surface Reactions in Carbon Monoxide and Oxygen Mixtures," *Journal of Thermophysics and Heat Transfer*, Vol. 14, No. 1, 2000, pp. 45–52. doi:10.2514/2.6488
[50] Howard, F., "Thermal Analysis Methods and Basic Heat-Transfer Data for a Turbulent Heating Flight Experiment at Mach 20 (Reentry F)," NASA TM-X-2282, 1971.

P. Tucker
Associate Editor